Open-system behaviour of magmatic fluid phase and transport of copper in arc magmas at Krakatau and Batur volcanoes, Indonesia

Andrea Agangi, Steven M. Reddy

Department of Applied Geology, Curtin University, 6102 Bentley, WA, Australia

Andrea.agangi@curtin.edu.au

Key words: copper, volcanic arc, degassing, sulfide melt, Krakatau, Batur

Abstract

The Sunda arc of Indonesia is an excellent example of how volcanic processes at convergent plate margins affect the distribution of metals and control the distribution of ore deposits. In this paper, we report microtextural observations and microanalytical data (SEM-EDS and LA-ICP-MS) of silicate and sulfide melt inclusions from fresh samples of volcanic rocks from the 2008 eruption of Mt Krakatau and 1963 eruption of Mt Batur, Sunda arc, Indonesia that bear implications on the concentration and transport of Cu and other chalcophile elements in mafic-intermediate magmas in arc settings. These multi-phase inclusions contain glass, amphibole and plagioclase, together with co-trapped apatite, magnetite, sulfides and lobed, drop-like Fe-oxide. We observed two stages of sulfide formation: 1) early-formed sulfide globules (pyrrhotite and intermediate solid solution), which derived from an immiscible sulfide melt and only occur as inclusions in phenocrysts; and 2) late-formed, irregular Cu-rich sulfides (intermediate solid solution to bornite), which were deposited in presence of an aqueous fluid, and are contained as fluid phase precipitates in vapour bubbles of melt inclusions and in vesicles, as well as finely dispersed grains in the groundmass. Microtextural observations and X-ray elemental maps show that interaction between sulfide globules and aqueous fluid resulted in partial oxidation and transfer of Cu between the fluid and the sulfide phase. A compilation of whole-rock analyses from the Sunda arc indicates that Cu reaches ~250-300 ppm in mafic samples ($SiO_2 \leq 52$ wt.%), and then suddenly drops with progressive fractionation to <50 ppm in intermediate-felsic samples. This behaviour can be explained by sulfide melt exsolution or degassing and scavenging of Cu occurring at various stages of magma fractionation (at MgO ~ 8 – 2.5 wt.%). These trends can be effectively modelled by sulfide saturation during fractional crystallisation at oxygen fugacities varying from fO_2 = FMQ +0.8 to FMQ +1.4. In contrast, LA-ICP-MS analyses of whole multi-phase melt inclusions hosted in olivine, pyroxene and plagioclase indicate variable Cu and S contents (Cu up to ~6000 ppm), which do not correlate with fractionation indicators (e.g. SiO_2, MgO, Rb), consistent with co-trapping of Cu-S phases with silicate melt. The highest Cu concentrations, Cu/S and incompatible trace elements (e.g. Rb) were measured in plagioclase, which crystallised over a wider range of melt compositions in comparison with olivine and pyroxene, and preferentially contains late-formed Cu-rich sulfides. These results underline the importance of mafic-intermediate magmas as sources of Cu in magmatic-hydrothermal ore deposits, and suggest that S-rich fluid is of primary importance in the transport of Cu in arc settings.

1. Introduction

The Sunda-Banda volcanic arc of Indonesia (Fig 1) is well endowed with Cu-Au-porphyry and epithermal deposits, such as Batu Hijau (Cooke et al. 2005; Arif and Baker 2004; Richards 2013). With more than 100 active volcanoes (Sutawidjaja 2009), this arc exemplifies how subduction-related magmatism can create the right conditions for ore metal transport and deposition (Sillitoe 2010; Hedenquist and Lowenstern 1994). The accepted hypothesis for ore formation at convergent plate margins involves the exsolution of a magmatic hydrothermal phase at shallow depths and scavenging of metals from a volatile-rich magma (Hedenquist and Lowenstern 1994; Sillitoe 2010). However, the precise mechanisms of ore formation are still unresolved, and the relative importance of different magmatogenic and tectonic processes is being debated (Jenner et al. 2015; Park et al. 2015; Wilkinson 2013; Blundy et al. 2015). Importantly, because porphyry Cu-(Au) deposits are typically associated with intermediate-felsic intrusions, the role of silicic magmas as sources of metals is widely accepted (Hedenquist and Lowenstern 1994). However, felsic magmas tend to be relatively depleted in Cu and Au, which is why a possible role for mafic magmas as sources of metals and S has also been proposed (Keith et al. 1997; Hattori and Keith 2001; Sun et al. 2004; Park et al. 2015).

One important type of processes invoked for the concentration of ore metals is the unmixing of sulfide (Fe-S-O) melts and aqueous fluids from silicate melts. Unmixing of liquid phases can occur at different stages during magma evolution and is typically accompanied by extreme geochemical fractionation, as elements partition differently between coexisting liquids with widely diverging physical-chemical characteristics (Davidson et al. 2005; Kamenetsky and Kamenetsky 2010). Because Cu and other chalcophile elements have a strong tendency to partition into sulfide melt with respect to silicate melt (Ripley et al. 2002), exsolution of a sulfide phase is considered as a crucial mechanism to extract chalcophile elements from a magma (Naldrett 1969). Magma saturation with respect to a sulfide phase can be potentially triggered by various processes, such as crystallisation and reduction of oxidised magmas induced by magnetite crystallisation or SO_2 degassing (Dilles et al. 2015; Tomkins et al. 2012; Sun et al. 2004). Some authors have inferred that magmas that experience extensive sulfide melt exsolution and chalcophile element depletion before volatile saturation are unlikely to preserve ore-forming potential (Richards 2013; Park et al. 2015). Thus, the formation of Cu-Au deposits hosted in arc volcanoes will be controlled by the enrichment of ore metals in the parent magmas (Sun et al. 2004), but also by the timing of sulfide saturation and fluid exsolution (Jenner et al. 2010; Park et al. 2015).

To investigate the behaviour of metals during magma fractionation, and the role of immiscible sulfide melts and aqueous fluids in metal transport and their mutual interaction, we have studied recent samples from the Sunda arc, namely from the 2008 eruption of Krakatau, south of Sumatra and from the 1963 eruption of Batur, Bali. Both volcanoes have been previously extensively studied, and the conditions of crystallisation and the depth of magma storage are well-constrained by

geophysical and petrological methods, offering a good framework to study the formation of sulfur phases during magma evolution. We report microtextural and microanalytical data (laser ablation LA-ICP-MS analyses) that provide evidence for immiscibility of both sulfide melt and a S-rich fluid. This evidence allowed us to assess the relative importance of immiscible sulfide melt and aqueous fluid phase in the concentration and transport of Cu and other metals (Ag, Sn, Zn, Mo).

2. Geological setting

Krakatau geological setting

Mount Krakatau is located at the intersection of an active fault and the NNE-SSW-trending volcanic line in the Sunda Strait (Nishimura et al. 1992; Harjono et al. 1989) (Fig 1). The Sunda Strait marks the transition from the Java trench to the east, characterised by frontal subduction, and the Sumatra trench to the north-west, characterised by oblique subduction (Agustan et al. 2012). This setting is associated with faulting and extension, which resulted in the deposition of an estimated 4 km thick marine succession (Mandeville et al. 1996). The Krakatau complex consists of four islands: Sertung, Panjang, Rakata and Anak Krakatau. The first three are the remnants after the caldera collapse that followed the 1883 eruption. This catastrophic eruption produced 12.5 km^3 dense rock equivalent of dacite pumice, and is estimated to have emitted 2.8 tg of S (Mandeville et al. 1996). Anak Krakatau was formed from the 1930s and is composed of lava and pyroclastic deposits (Sutawidjaja 2009).

Microseismic studies have identified three boundaries interpreted to mark the contact between major lithological contacts: the first boundary, at around 4 km depth, is interpreted as the contact between sediments and a granitic basement, the second, at around 9 km, as the boundary with mafic intrusive rocks, and the third marks the Moho at around 22 km depth (Harjono et al. 1989). Two magma storage domains have been identified based on locations of seismic attenuation zones, a large reservoir at a depth of 22 km and isolated magma pockets at 9 km underneath Anak Krakatau (Harjono et al. 1989; Jaxybulatov et al. 2011). Petrological estimates based on mineral-melt equilibria indicate crystallisation of clinopyroxene between 7 and 12 km, and plagioclase crystallisation at both sub-Moho (23 – 28 km) and upper crustal (3 – 7 km) depths (Dahren et al. 2012). Further, Mandeville et al. (1996) estimated melt inclusions to have degassed Cl at around 100 MPa in dacitic pumice produced by the 1883 eruption.

Direct information on the lithologies underlying Krakatau comes from the observation of xenoliths in the products of various eruptions, which include metasedimentary cordierite-bearing rocks, mudstone, diorite and granite (Gardner et al. 2013; Ōba et al. 1992). The Anak Krakatau eruption products form a rather homogeneous group, with most samples having basaltic andesite composition, together with minor basalt and andesite (Dahren et al. 2012; Gardner et al. 2013). Since 1988, Anak Krakatau has intermittently erupted basaltic andesite producing strombolian eruptions and lavas (Gardner et al. 2013). One of these eruptive events occurred between October

2007 and August 2008. This eruption, sampled for this study, was characterised by strombolian activity with ash columns 1 km high, producing pyroclastic deposits and lava flows (Agustan et al. 2012).

Batur geological setting

The Batur volcanic field is located in the north of the Island of Bali. The crust beneath the volcanic field is about 20 km thick (Curray et al. 1977). The oldest volcanic rocks exposed on Bali are pillow basalts of Late Pliocene age (Wheller and Varne 1986). The evolution of the volcanic field was marked by two major caldera-forming eruptions and intervening stratovolcano-forming eruptions (Watanabe et al. 2010; Sutawidjaja 2009), and can be subdivided into six episodes (Reubi and Nicholls 2004b): 1) building of a basaltic stratovolcano starting at 510 ka (Wheller and Varne 1986); 2) caldera collapse and emplacement of dacitic ignimbrite at 29 ka (Sutawidjaja 2009); 3) formation of an andesitic to dacitic lava dome; 4) second caldera collapse and emplacement of andesitic to dacitic ignimbrite at 20 ka (Sutawidjaja 1990; 2009; Marinelli and Tazieff 1968); 5) andesitic to dacitic explosive activity; 6) building of the historically active basaltic andesite stratovolcano in the second caldera. Stage 6 includes multiple small-volume mafic to intermediate eruptions, the largest of which occurred in 1963 (Wheller and Varne 1986). This eruption was sampled for this study.

Products of volcanic eruptions at Batur have been subdivided according to their mineralogy (Reubi and Nicholls 2004a) into four groups: 1) plagioclase-olivine suite that comprises basalt only, 2) plagioclase-orthopyroxene-clinopyroxene-amphibole suite (andesite), 3) plagioclase-clinopyroxene-orthopyroxene suite (basalts to andesite), and 4) plagioclase-olivine-clinopyroxene suite (basaltic andesite to dacite). The olivine-clinopyroxene-bearing group has become progressively predominant over time during the last thousands of years, and has dominated the historical eruptions (Reubi and Nicholls 2004a). The four series are interpreted to have formed by fractionation under variable pressure (2 – 7 kbar) and variable water contents (1 – 3 wt.%) with minor or no crustal assimilation (Reubi and Nicholls 2004a).

3. Sample preparation and analytical techniques

We investigated samples from the 2008 eruption of Anak Krakatau, collected in February 2009 from the area immediately surrounding the crater, and from the 1963 eruption of Batur. Samples were prepared as polished thin sections and rock chip mounts. In addition, portions of the samples were crushed in a steel mortar and sieved. Crystals of plagioclase, pyroxene and olivine were hand-picked under a binocular from the size fractions between 0.5 and 1.5 mm. Grains were then mounted in epoxy, ground by using non-water-based lubricants and polished. Observations were made by optical microscopy and back-scattered electrons (BSE) and secondary electron (SE) modes of scanning electron microscopy (SEM). Mineral compositions and XR elemental maps were obtained with a Mira Tescan field emission electron microscope (FE-SEM) equipped with an energy-dispersion

spectroscopy (EDS) detector at Curtin University. During analyses, an acceleration of 20 kV and << 1 µm spot size were applied. The calculated accuracy of analyses is ~0.1 wt.% for all elements.

Laser ablation ICP-MS

Unexposed melt inclusions hosted in plagioclase, olivine and pyroxene were analysed by LA-ICP-MS by ablating whole multi-phase inclusions, according to the method of Halter et al. (2002). This technique allows to avoid heating in the laboratory to homogenise the inclusions, which can cause mobilisation of the most volatile elements, and notably Cu and Ag. Major and trace elements were analysed simultaneously using a Coherent CompEX solid state 193 nm laser, and an Agilent 7700 quadrupole mass spectrometer at Curtin University. Ablation was performed at 10 Hz repetition rate, 50 µm spot size and approximately 3 J/cm^2 fluence. During spot analyses, 20 seconds of background acquisition were followed by 50-60 s ablation. Masses ^{23}Na, ^{24}Mg, ^{27}Al, ^{28}Si, ^{31}P, ^{34}S, ^{39}K, ^{43}Ca, ^{49}Ti, ^{51}V, ^{55}Mn, ^{57}Fe, ^{59}Co, ^{60}Ni, ^{65}Cu, ^{66}Zn, ^{75}As, ^{77}Se, ^{85}Rb, ^{88}Sr, ^{89}Y, ^{90}Zr, ^{93}Nb, ^{95}Mo, ^{107}Ag, ^{118}Sn, ^{121}Sb, ^{137}Ba, ^{139}La, ^{140}Ce, ^{147}Sm, ^{141}Pr, ^{146}Nd, ^{157}Gd, ^{166}Er, ^{169}Tm, ^{175}Lu, ^{157}Gd, ^{163}Dy, ^{172}Yb, ^{197}Au, ^{206}Pb, ^{232}Th were analysed for 0.02 to 0.03 s each. Quantification of element concentrations was obtained using glass NIST 610 (Jochum et al. 2011) and Al, which varies over a limited range in whole-rock analyses, was used to recalculate the proportions between melt inclusions and host minerals.

4. ***Sample description, mineral chemistry and conditions of crystallisation***

Krakatau

The samples are composed of highly vesicular scoria, containing phenocrysts of plagioclase, clinopyroxene (pleochroic green-brown, augite) and orthopyroxene set in a fine-grained glass-bearing groundmass (Fig 2A). Ti-magnetite and apatite are present as accessory phases in the groundmass and as inclusions in phenocrysts. Plagioclase and pyroxene also form aggregates of several crystals (glomerophyric texture), and microgranular enclaves of plagioclase and have been observed. Plagioclase has variable textures and shows evidence of strong resorption, resulting in well-developed sieve texture (Fig 2B). In some crystals, a round, relatively massive-textured core is rimmed by sieve-textured plagioclase. In other crystals, sieve-textured plagioclase is rimmed by a massive textured overgrowth. Plagioclase composition is mostly high-Ca labradorite to bitownite (An63-88), although in embayments and melt inclusions, the anorthite content can be as low as An35.

The most Ca-rich plagioclase compositions (An >79) overlap with compositions expected to crystallise from basalt and basaltic andesite, calculated using whole-rock compositions from Anak Krakatau with SiO_2 < 55 wt.% (Camus et al. 1987; Gardner et al. 2013) and assuming K_D(Ca-Na) = 0.27 (Putirka 2008) (Additional Fig 1). More Ca-poor compositions (An 63-78) are calculated to be in equilibrium with andesite (using whole-rock analyses of the 1981 eruption, Camus et al. 1987;

Gardner et al. 2013). Even more Ca-poor plagioclase (An <63) was reported from phenocrysts in dacite in previous studies (Mandeville et al. 1996; Dahren et al. 2012), and analysed in melt inclusions in this study.

Orthopyroxene from Krakatau has Mg# (Mg/(Mg + Fe), molar) of 73 – 75, clinopyroxene has Mg# of 73 – 77 (two outlying analyses have Mg# 60 and 68). Previous analyses of pyroxenes from rocks ranging from basalt to dacite indicate that clinopyroxene spans the Mg# range 66 – 78 (Camus et al. 1987; Mandeville et al. 1996; Dahren et al. 2012), and orthopyroxene the range Mg# 66 – 76 (pigeonite extends to Mg# 61). Mg# of pyroxene between 70 and 79 are expected from basalt and basaltic andesite melt (average of whole-rock analyses with SiO_2 <55 wt.%), assuming a K_D(Mg-Fe) of 0.27. The pyroxenes in our samples are, therefore, interpreted as being in equilibrium with basalt and basaltic andesite melts. Pyroxenes with significantly lower Mg# (lesser than ~70) found in previous studies are interpreted as having crystallised from andesite and dacite (Camus et al. 1987; Gardner et al. 2013).

Batur

The sample is a vesicular lava with phenocrysts of plagioclase, clinopyroxene and olivine, locally forming glomerocrysts, set in a fine-grained groundmass of microlithic plagioclase, Ti-magnetite and glass (Fig 2C, D). Ti-magnetite and acicular apatite also occur as inclusions in phenocrysts. Plagioclase phenocrysts have broad sieve-textured domains, which are in several cases rimmed by narrow, more massive-textured overgrowths, and have compositions varying from An43 to An86 (Additional Fig 1). The most Ca-poor portions were found rimming embayments and melt inclusions. Cracks across plagioclase are in some cases lined with amphibole.

Previously published plagioclase analyses from Batur span a wide interval (An~30-90), with wide variations occurring even within single rock types and between crystals in single samples (Reubi and Nicholls 2004a; 2005). Plagioclase analyses with the highest anorthite content (An ≥78) overlap with the compositions expected for basalt and basaltic andesite (whole-rock analyses with SiO_2 <55 wt.%; (Reubi and Nicholls 2004a; 2005; Wheller and Varne 1986). The other plagioclase analyses having compositions (An <78), are expected for plagioclase in equilibrium with andesite and dacite. Olivine has Mg# (forsterite content) = 62 – 69 and contains small amounts of Ca (up to 0.3 wt.%). Previous olivine analyses indicate wide compositional ranges (Mg# ~30 – 80 overall) and large overlap between crystals from samples of basaltic to dacitic composition (Reubi and Nicholls 2004a). Olivine phenocrysts having Mg# = 61 – 80 are in equilibrium with a basalt and basaltic andesite melt. Clinopyroxene has Mg# 60 – 73). These compositions appear to be in equilibrium with basaltic andesite and andesite.

Krakatau and Batur – Thermobarometric estimates

Geothermobarometry methods have been applied to our mineral analyses and previous analyses of phenocrysts to estimate the P-T conditions of crystallisation and sulfide entrapment (Table 1). The observed plagioclase compositional variations and textural features at Mt Batur and Krakatau confirm previous analyses, and are consistent with protracted crystallisation from melt of varying composition at different P-T conditions. In contrast to plagioclase, pyroxene and olivine have narrower compositional ranges in our analyses and formed under relatively constrained P-T conditions. This matches narrower ranges of olivine- and pyroxene-hosted melt inclusion compositions in comparison to plagioclase analysed in this study.

*5. **Whole-rock compositions***

A dataset representative of the whole Sunda arc (approximately 1900 analyses) has been selected from the website http://georoc.mpch-mainz.gwdg.de/ and from Sutawidjaja (2015) (plotted in Fig 3). Of these, approximately 250 whole-rock analyses and 37 groundmass glass and glass inclusion analyses are available for Batur and Krakatau volcanoes. The analyses have been selected as having SiO_2 = 45 – 80 wt.%, loss on ignition < 10 wt.%, and $Al_2O_3/(Na_2O+K_2O+CaO)$ < 1.5, so that silicified, strongly altered and carbonate-rich samples have been avoided. Analyses from Krakatau and Batur span similar concentration ranges of all major element oxides. SiO_2 ranges from 48 to 74 wt.%, corresponding to basalt to rhyolite in the total alkalis vs. SiO_2 diagram. At Krakatau and Batur, K_2O increases steadily with increasing SiO_2 and most analyses plot in the mid- to high-K field (Fig 3). In the Sunda arc as a whole, a series of ultra-K mafic-intermediate samples is also present. Glass analyses from Krakatau and Batur plot towards the high SiO_2 end of whole-rock compositions and match the lowest CaO and FeO whole-rock analyses, indicating a relatively evolved composition. Glass analyses are mostly andesite to rhyolite in the total alkali vs. SiO_2 diagram. The analyses show variable Fe-increasing trends in the FeO(Tot) – MgO – (Na_2O+K_2O) plot of Kuno (1968). In this plot, analyses from Batur and Krakatau have some of the highest enrichments in Fe and straddle the boundary line between calc-alkaline and tholeiitic trends (Fig 3). The concentrations of TiO_2 and MnO vs. SiO_2 (and MgO) also indicate variable trends, which are likely indicative of the variable timing of magnetite crystallisation. In some samples, such as the ones from Krakatau and Batur, TiO_2 and MnO increase with SiO_2 up to ~56 wt.% (and MgO 2.0 – 2.5 wt.%), and then decrease for higher SiO_2 contents (Fig 3). In other analyses from the Sunda arc, however, TiO_2 peaks at lower SiO_2 concentrations (50 – 51 wt.%, corresponding to ~4.2 wt.% MgO), or even decreases continuously. Copper concentrations also have considerable scatter in plots vs. SiO_2 or MgO (Fig 3). The variability of Cu concentrations is greatest at MgO ~2.5 – 4 wt.% (or SiO_2 ~52 – 56 wt.%), where Cu spans from ~10 to ~300 ppm. At lower MgO, Cu drops significantly to < 50 ppm, although the most evolved samples contain significantly higher and scattered Cu concentrations. A similar distribution may exist for Mo, although the scarcity of analyses of Mo in mafic samples makes this observation contentious. At SiO_2 > 52 wt.% (MgO < 4 wt.%) Mo positively correlates with SiO_2 and incompatible elements, Rb, Y and La, indicating that it was progressively concentrated in the melt with progressive fractionation.

6. Silicate melt and sulfide inclusion description

Melt inclusions were found in all phenocryst phases: plagioclase, pyroxene and olivine, as well as magnetite. In samples from both Krakatau and Batur, melt inclusions contain variable proportions of glass, one or multiple bubbles, Ca-amphibole, plagioclase, magnetite, apatite and different (Fe-Cu-) sulfide phases (Fig 4). Apatite forms short euhedral prisms (Fig 4B) or needles extending from the melt inclusions into the host phase. The variable, and locally very high, abundance of apatite and magnetite suggests that these phases were trapped with melt during crystal growth, rather than having crystallised from the melt after entrapment. Calcium-amphibole is abundant in melt inclusions, despite being absent from the phenocryst assemblage (Fig 4C, D). Plagioclase-hosted melt inclusions are mostly crystallised, and several of these have a concentric distribution of minerals, with Na-rich plagioclase forming on the inclusion walls and amphibole towards the interior of the inclusions (Fig 4C). This amphibole is associated with bubbles, and in some cases has a vesicular microtexture, attesting to the fluid-saturated nature of the trapped melt at the moment of amphibole crystallisation (Fig 4D). Melt inclusions contain a single bubble or, in some cases, a large number of small, µm-scale bubbles. In several cases, these bubbles contain fine-grained precipitates of Fe-sulfide, Cu-Fe-sulfide, Fe-oxide and silicates (Fig 4B, 4C, Fig5). Bubbles constitute a variable proportion of the whole inclusion, from ~3 to ~20 vol.%, suggesting that not all bubbles are the result of post-entrapment shrinkage, and they were partly formed by heterogeneous entrapment of fluid and melt.

Two types of sulfides were found in melt inclusions: 1) globules of pyrrhotite ±intermediate solid solution (chalcopyrite-cubanite), up to ~ 100 µm in size (Fig 4E, Additional Fig 2A, B); 2) small (µm-scale) and irregular, Cu-rich sulfides occurring in melt inclusion bubbles and in contact with amphibole, and in the groundmass (Fig 4C, D, Additional Fig 3). Round sulfide globules occur as inclusions in pyroxene, plagioclase, olivine and Ti-magnetite, but they are absent from the groundmass. Sulfide globules coexist with glass, silicates (mostly plagioclase and amphibole) and magnetite (Additional Fig 2A, B). In sulfide globules, Cu-sulfide typically rims pyrrhotite, and occurs in contact with glass (Additional Fig 2A). The round section of these sulfide globules is consistent with formation as an immiscible liquid and the presence of pyrrhotite and intermediate solid solution is typically interpreted as resulting from crystallisation from sulfide melt upon cooling (Prichard et al. 2004). Some of these sulfide globules appear as cracked and altered (Fig 6). Altered portions developed from micro-cracks and on the rim of sulfide globules, and are enriched in O and Cu, as shown by X-ray element maps (Fig 6). Some of these partially oxidised sulfide globules are accompanied by numerous small bubbles developed in the surrounding glass (Fig 6B).

EDS analyses of sulfide globules plotted in the Cu-S-Fe triangular diagram fall close to pyrrhotite compositions and near intermediate solid solution (or chalcopyrite-cubanite) (Fig 7). Analyses of pyrrhotite indicate near-pure Fe-S composition (pyrrhotite $Fe_{0.84}S$), with Cu contents < 4.2 wt.%, and small amounts of Ni (up to 0.7 wt.%). Very Cu-rich sulfide (chalcopyrite to bornite-

chalcocite [Cu_2S]) compositions were found in small irregular grains in plagioclase-hosted melt inclusions in contact with amphibole. Minor amounts of round, lobed or elongate, drop-like Fe-oxide blebs occur as inclusions in plagioclase, olivine and pyroxene, both at Krakatau and Batur (Additional Fig 2D-F). These Fe-oxide blebs were trapped as single-phase inclusions or co-trapped with melt, sulfide globules and apatite. EDS analyses of these grains indicate variable Ti contents (from below detection limit to 6.5 wt.%. An anhedral Fe-O-(S) anhedral phase was found lining vesicles at Krakatau (Additional Fig 2C), which contains minor amounts of Ti (<0.6 wt.%).

7. Melt inclusion analyses

LA-ICP-MS melt inclusion analyses at Batur and Krakatau span a wide range of major element oxide compositions (SiO_2 = 49 – 66 wt.%) and largely overlap with whole-rock analyses (Fig 3, Additional Table). Melt inclusion analyses mostly plot in the mid- to high-K field, in good agreement with available whole-rock analyses. Positive correlations found between Y, rare earth elements (REE), Zr, Nb and Rb indicate that these elements all behaved as incompatible elements. The highest concentrations of incompatible trace elements were measured in plagioclase (e.g. Rb up to 70 ppm), indicating that plagioclase trapped some of the most chemically evolved melt at late stages of crystal fractionation. Copper concentrations are variable (up to ~6700 ppm) (Fig 8) and do not correlate with any other element. The highest concentrations of Cu, Zn, Mo, Ag and Sn and the highest Cu/S and Cu/Ag were measured in plagioclase-hosted melt inclusions. The ratio Cu/S in clinopyroxene and olivine-hosted melt inclusions is 0.1 – 0.5, reflecting the trapping of a mixture of pyrrhotite and chalcopyrite, whereas in plagioclase-hosted melt inclusions it is highly variable and up to 10 (Fig 8). Silver concentrations are up to 1.2 ppm and do not correlate with other elements. Zinc is present in concentrations up to 175 ppm and correlates positively with Mn, V and Co. Both Sn and Mo (up to 3 ppm) have positive correlation with incompatible elements (e.g. Rb and Zr) (Fig 8). In all the analyses Au content is below detection limit. Inspection of the ablation signals indicates that Cu and Ag are heterogeneously distributed, with significant peaks occurring at narrow intervals during analyses (Fig 9), which is compatible with the observation of Cu-bearing phases in exposed melt inclusions. In contrast, the signal of Zn and Mo is homogeneous throughout the melt inclusions.

8. Discussion

8.1 Cu behaviour during magma crystallisation and sulfide melt exsolution

Chalcophile elements have a strong tendency to partition into sulfide melts at the equilibrium with a silicate melt (Jugo et al. 2005), so that saturation of sulfide will strongly control their distribution during fractional crystallisation. Indications on the behaviour of Cu during magma evolution in the Sunda arc can be achieved by modelling fractional crystallisation based on whole-rock compositions. Major element variations during crystallisation of the main mineral phases (olivine, pyroxene, plagioclase, Fe-oxide) have been modelled using the software Petrolog3 (Danyushevsky and Plechov 2011). This software combines several published models to calculate the

conditions of stability of minerals and the fractionation path during the crystallisation of a magma. Simulations of simple fractional crystallisation have been carried out at the pressure of 2 kbar, 1 wt.% H_2O and fO_2 of 1 Log unit above the fayalite-magnetite-quartz buffer (FMQ +1), using a basalt with 10.8 wt.% MgO and 70 ppm Cu as starting composition.

This model was then modified to take into account the effect of sulfide saturation by using the equation of Mavrogenes and O'Neill (1999), which describes the solubility of sulfide in silicate melts as a function of temperature, pressure and fO_2. These calculations were run at 2 kbar, and at the temperatures predicted by Petrolog3 during fractionation. For S, a concentration of 1000 ppm has been used as the initial concentration for the calculations. This is the approximate average S concentration measured by deHoog et al. (2001) in mafic melt inclusions from west Java, and is compatible with S in olivine-hosted melt inclusions from Bali (Self and King 1996). To model the extraction of Cu during sulfide melt separation, a sulfide melt-silicate melt distribution coefficient Kd(Cu) of 1000 has been used. Although this distribution coefficient is known to vary as a function of oxygen fugacity, we assumed it to be constant for the relatively narrow range of fO_2 considered in our model (Patten et al., 2013; Li and Audétat, 2012; Kiseeva and Woods, 2013). The model predicts that saturation will be reached at various degrees of fractionation (and MgO concentration), depending primarily on fO_2 (Fig 10). At oxygen fugacity of FMQ +0.8, saturation occurs at around 8 wt.% MgO (and 95 ppm Cu), whereas at FMQ +1.4 saturation occurs at around 3.6 wt.% MgO (290 ppm Cu). The Cu depletion during sulfide fractionation describes curved trends that match well the observed distribution of available analyses. Thus, most of the distribution of analyses in the Sunda arc can be described by varying fO_2 over a narrow range (FMQ +0.8 to FMQ +1.4). Decreasing pressure will increase S solubility, but even pressures as low as 0.1 kbar only appear to have a minor effect on the MgO values at sulfide saturation. It should be also noted that, although Cu depletion is here modelled as due to a sulfide melt, S degassing may have also played a role. The vapour-silicate melt partition coefficients are not well constrained, but values of ~7 have been proposed in mafic magmas (Berlo et al., 2014). Despite the fact that arc magmas are generally considered to have high fO_2 in comparison to magmas formed in extensional settings, the finding of sulfide minerals in lithospheric mantle xenoliths and in magmatic cumulates in arc environments (Richards 2015) suggest that arc magmas can exsolve sulfide melt throughout their crystallisation history.

The degree of Fe-enrichment during fractional crystallisation is believed to be the consequence of the timing of magnetite saturation (Ariskin 1996): delayed magnetite saturation would result in Fe-enriching trends, whereas early magnetite fractionation would deplete the melt in Fe. This is also reflected in the variable Ti- and Mn- enriching trends observed in plots versus SiO_2 or MgO. This, in turn, may be related to the fO_2 of the magma, as magnetite stabilisation will be favoured at high levels of oxidisation. If the Sunda arc whole-rock analyses are distinguished into two groups based on the FeOT/(FeOT+MgO) values in a plot versus SiO_2 (Fig 3), the analyses with the highest Cu concentrations also show the highest values of FeOT/(FeOT+MgO). This apparent co-occurrence of magnetite and sulfide saturation may be a consequence of the Fe^{3+}/Fe^{2+} decrease

induced by magnetite crystallisation as previously proposed (Sun et al. 2004; Jenner et al. 2010). To fully account for the role of magnetite is beyond the scope of this paper. However, we note that magnetite occurs as inclusions in different phenocrysts, implying formation at different stages, and both sub- to euhedral magnetite grains and irregular Fe-oxide blebs have been observed. Given the lobed, locally necked, droplet-like shape of some Fe-oxide blebs (Additional Fig 2), we propose that these grains may have formed from an immiscible Fe-oxide melt. Fe±(Ti-P)-oxide melt can form by immiscibility from mafic to felsic silicate melts (Hurai et al. 1998; Kamenetsky et al. 2013), or by exsolution from Fe-S-O melts, in a process termed "second segregation" (Desborough et al. 1968; Larocque et al. 2000). These melts can extract Fe^{3+} from the magma, thus affecting its fO_2. Available estimates of fO_2 at both Krakatau and Batur indicate relatively low levels of oxidisation of mafic and intermediate magmas. Mandeville (1996) estimated the fO_2 of pre-1883 andesite at levels around FMQ +1 based on two Fe-Ti-oxides oxygen barometry. At Batur, estimates of fO_2 in mafic and intermediate rocks are not available in the literature, and the absence of two Fe-Ti-oxides prevented such estimates in our samples. Application of the oxygen geobarometer of Canil and Fedortchouk (2001), which is based on the distribution of V between olivine and melt, to olivine-melt inclusion pairs in our analyses gives an average fO_2 value of NNO (nickel-nickel oxide) +0.0 ±0.7 (approximately FMQ +0.7).

8.2 Fluid-assisted deposition of Cu-rich sulfides

In addition to pyrrhotite-bearing globules, small (µm-scale) and irregular Cu-rich sulfide grains spanning in composition from intermediate solid solution to bornite and Cu_2S have been observed in bubbles of melt inclusions, in the ground mass and in vesicles (Fig 4B). Precipitation of Cu-rich sulfide at high H_2O activity is also illustrated by some melt inclusion textures, which show how crystallisation of plagioclase on the inclusion walls caused the concentration of volatile components (H_2O, S, Cu) in the residual melt until saturation prompted vesiculation and amphibole precipitation (Fig 4C, D, Additional Fig 3). Cu-rich sulfide grains formed at this stage, in the presence of a fluid phase. The entrapment of this fluid phase in phenocrysts, especially plagioclase, is reflected by the strongly variable Cu content of melt inclusion analyses. The preferential entrapment of Cu-rich sulfides in plagioclase can be explained by the fact that this mineral crystallised over a wide interval of melt composition (Additional Fig 1) and temperatures (Table 1), and shows evidence for resorption and embayments, which would have favoured fluid nucleation and entrapment. In addition to timing, the preferential entrapment of this fluid in plagioclase may be explained by the role of an increasing amount of water on plagioclase stability. Sieve textured plagioclase, which host many of the analysed melt inclusions, has been interpreted as the consequence of mixing with a more mafic melt, and as the result of decompression under water-undersaturated condition (Nelson and Montana, 1992). In addition, water is known to suppress the stability of plagioclase in comparison to olivine and pyroxene (Pichavant and MacDonald, 2007), thus the ingress of water through a fluid may have contributed to the destabilisation of plagioclase. Part of this fluid, which would have carried S and Cu as well, could have then been preferentially trapped in embayments

formed in plagioclase by dissolution. Interaction of this fluid with sulfide globules can be observed in cases where the host mineral cracked and the inclusions became open to the surrounding melt that had become undersaturated in S following, for example, decompression and degassing, or influx of an oxidising fluid. This interaction resulted in alteration of sulfide globules, thus explaining their absence in the rock matrix. Development of effervescence around sulfide globules (bubbles occurring in the silicate glass, Fig 6B) may also be the consequence of destabilisation of sulfide globules and release of S fluid into the surrounding melt. Although breakdown of sulfide caused by an exsolved aqueous fluid is certainly possible, the distribution of bubbles around the sulfide (Fig 6) is an indication of their formation mechanism. A random distribution of bubbles in the glass would argue against a link with the sulfide. Instead, the spatial correlation of bubbles with the sulfide suggests that bubbles originated from it. We interpret this texture as an arrested reaction of sulfide destabilisation. A similar process has been proposed to explain the "frothy" sulfide textures of Larocque et al. (2000), and is the expected consequence of S undersaturation caused by an increase of O fugacity in the magma.

The occurrence of different generations of sulfide phases is similar to what was found at Mt Pinatubo, where sulfides phases have been described as: 1) globular Ni-bearing pyrrhotite and chalcopyrite hosted as inclusions in early phenocrysts (olivine, augite) of basalt and andesite, and 2) irregular Cu-rich (up to 53 wt.% Cu) sulfides occurring as inclusions in late-formed phenocrysts and glass of basalt, andesite and dacite (Hattori 1993; de Hoog et al. 2004). Hattori (1993) proposed a late deposition of Cu-rich sulfides in dacite from SO_2-rich supercritical fluids released by underlying mafic magmas. In contrast, Di Muro et al. (2008) proposed that S-Cu-bearing aqueous fluid was released from the dacite upon mixing of mafic and dacitic magma. The conditions of introduction of this fluid can be constrained based on textures and thermobarometric estimates. Plagioclase, which preferentially entrapped Cu-sulfide precipitated from this fluid, may have crystallised at temperatures as low as 980°C at Krakatau and 950°C at Batur. The alteration of sulfide globules along cracks (Fig 6, Additional Fig 2) indicates that fluid introduction occurred at temperatures lower than sulfide crystallisation (~1000°C) (Naldrett 1969), whereas the formation of bubbles in the melt around some sulfide globules indicates that sulfide destabilisation must have happened at magmatic temperatures, i.e. above the glass transition temperature, and shortly before eruption and quenching. Further, the presence of sulfide lining vesicles indicates S degassing and sulfide deposition continued until syn- to post-eruption.

8.3 Introduction of S-O fluid and progressive oxidation of sulfide globules

The destabilisation of magmatic sulfides is typically interpreted as indicating an increase of fO_2 to values exceeding the sulfide-sulfate redox boundary (approximately FMQ +1 to +2; Jugo et al. 2005). Increase of fO_2 can be achieved through different open-system or closed-system processes. Since Fe^{3+} is more incompatible than Fe^{2+} in olivine and pyroxene, crystal fractionation will lead to progressive increase of Fe^{3+}/Fe^{2+} and thus, oxidation of the magma. Volatile saturation during

fractionation and degassing ("self-oxidation"; Bell and Simon 2011) can also increase the oxidation state of a magma. Loss of SO_2-rich vapour from the magma would cause oxidation of pyrrhotite globules according to the reaction $FeS(Po) + 3/2O_2 = FeO(l) + SO_2(v)$ (Candela and Holland 1986). Another mechanism is the influx of SO_2 from an external source, especially a mafic and relatively anhydrous one, which would tend to degas high SO_2/H_2S fluids (Hattori 1993). Alternatively, disproportionation of SO_2 may lead to deposition of both sulfide and sulfate, without the need of oxidation of the bulk magma (de Hoog et al. 2004). Mixing with an oxidised magma, such as wet, cool and high-fO_2 intermediate-felsic magma (Kress 1997), is also an effective way of modifying the oxidation state, while introducing fluids and fluid-mobile elements into a magma. Apart from mixing with felsic magma, for which we have no obvious evidence in our samples, all these processes are possible, although open-system fluxing of SO_2 fluid through the magma is considered a particularly important process at Batur and Krakatau, as detailed in the following paragraphs.

In the Sunda arc, high-SO_2 fluid emissions have been measured at several volcanoes (Bani et al. 2015; Aiuppa et al. 2015), even during non-eruptive periods, implying continuous S degassing at depth. Recent UV absorption spectroscopy observations of gas emissions at Krakatau have underlined strong SO_2 emissions (190 t/day in 2014) during quiescence periods (Bani et al. 2015), whereas at Bromo, east Java, S emission was estimated to consist of 166 t/day SO_2 and 25 t/day H_2S (Aiuppa et al. 2015). At Krakatau and several other volcanoes in the southeast Asian region and elsewhere, a "sulfur excess" has been observed during eruptions. This term refers to the phenomenon involving S emissions that far exceed what is expected from the solubility of S in the erupted magma, and may be due to the presence of a "pre-eruptive" S fluid in the magma chamber, or destabilisation of magmatic sulfate and sulfide (Mandeville et al. 1998; Wallace 2001; Pallister et al. 1992). Sulfur degassing at Krakatau was also inferred by melt inclusion analyses and $\delta^{34}S$ values. High $\delta^{34}S$ values of whole-rocks at Krakatau have been interpreted to indicate extensive open-system degassing of S, and the fact that even sulfide globules have high $\delta^{34}S$ indicates deep degassing, possibly at depths of 4 – 5 km. In general, mafic magmas are known to degas SO_2, together with H_2O and CO_2, during ascent due to decompression and crystallisation (Borisova et al. 2014). At Mt Pinatubo, formation of high-S apatite is also thought to be due to the influx high-S fluids (Van Hoose et al. 2013). Bubbles of S-rich fluid deriving from deep mafic magma can accumulate in the magma chamber and then be released, either abruptly during eruptive events, or continually during non-eruptive periods (Shinohara 2008; Edmonds et al. 2010).

We propose that an oxidised Cu-bearing S-rich fluid was fluxed through magma that had previously undergone sulfide segregation and Cu depletion. This resulted in the destabilisation of any sulfide globules that were not trapped and shielded by phenocrysts, and transfer of Cu between magma batches, with the formation of Cu-rich sulfide in melt inclusion bubbles, vesicles and in the groundmass. The compositional differences (e.g. Cu/S, Cu/Ag) between the two generations of sulfides suggest that Cu was added from an external source. Therefore, we infer that this S-rich fluid was originated from a separate (deeper) magma batch, and was able to transport Cu (and possibly

other metals) towards the surface. Textural evidence indicates that this fluid was present at both pre-eruption and syn-eruption stages, and may have been instrumental in triggering the eruption (Pallister et al. 1992).

8.4 Contrasting behaviour of transition metals (Cu, Ag, Zn, Mo, Sn)

In melt inclusion analyses, Cu and Ag have erratic concentrations in plots versus SiO_2 and incompatible elements, and show heterogeneous distribution in time-resolved LA-ICP-MS signals, which indicates preferential distribution in sulfide phases, confirming the strong chalcophile behaviour of Ag (Kd(Ag) ~1100 – 1300; Jenner et al. 2010; Li and Audétat 2012; Patten et al. 2013). Cu/Ag values are ~1000 in early-trapped olivine- and pyroxene-hosted melt inclusions, and up to 10 times higher in plagioclase-hosted melt inclusions (Fig 8). This suggests a preferential mobilisation of Cu relative to Ag in the later stages of fluid-assisted sulfide formation. Molybdenum and Sn are also expected to behave as moderately chalcophile elements (Kd(Sn) of 11; Patten et al. 2013). In whole-rock analyses, Mo and Sn reach the highest concentrations in samples with MgO >4 wt.%. Therefore they may have behaved similarly to Cu during sulfide saturation, although the limited analyses available for mafic samples make this interpretation contentious. At more evolved compositions (MgO < 4 wt.%), Mo and Sn increase with decreasing MgO and correlate with incompatible elements (Rb, Y, Zr, Fig 3, Fig 8). The homogeneous distribution in LA-ICP-MS time-resolved spectra suggests that these metals were mostly hosted by silicate melt, rather than fluid or sulfide melt, at the moment of trapping. The behaviour of Zn, which contrasts with Cu, reflects the strong preference of Cu to bond covalently with S, whereas Zn has a preference for ionic bonding in silicate melt (Simon and Ripley 2011; MacLean and Shimazaki 1976). This is consistent with a sulfide-silicate melt distribution coefficient Kd(Zn) of <1 reported by some authors (MacLean and Shimazaki 1976; Li and Audétat 2012). In addition, the positive correlation between Zn and Mn in our samples (Fig 8) is compatible with the observation of Zn contents up to thousands of ppm in magnetite crystallising from both silicate and sulfide melts (Dare et al. 2012), and suggests a control by magnetite crystallisation (magnetite-silicic melt Kd(Zn) = 15 was reported by Ewart and Griffin, 1994).

8.5 Role of S in the transport of Cu

High volatility of Cu is clearly shown in natural Cl-bearing fluids (Heinrich et al. 1992) and strong enrichment of Cu and Au in fluids coexisting with silicate melts from mineralised igneous rocks (Cu porphyry deposits) has been measured (Audétat et al. 2008). In addition to Cl, experiments and observations of natural samples have shown that also S can significantly increase the solubility of Cu (and Au) in magmatic fluids, and in particular vapours in comparison to brines (Pokrovski et al. 2015; Nagaseki and Hayashi 2008; Zajacz and Halter 2009). Further, the fact that sublimates from vapours at volcanoes producing basaltic magmas are richer in Cu compared to sublimates from felsic volcanoes (Williams-Jones and Heinrich 2005), seems to indicate that this process is especially effective for mafic magma-derived fluids. Open-system flushing of S fluids through magmas (deep degassing) would cause interaction of fluid with large volumes of magma, leading to disequilibrium

fractionation of Cu into these fluids, and effective scavenging of metals from magmas and from sulfides. Thus, the high and scattered Cu concentrations in some intermediate-felsic whole-rock samples in our dataset (up to 150 ppm, Fig 10), which are not accounted for by sulfide melt exsolution, may be due to this type of fluid-assisted processes.

9. Summary and conclusions

The study of silicate and sulfide melt inclusions in samples from Mt Krakatau and Batur indicates that Cu was separated during two stages of sulfide formation. Stage 1 involved the exsolution of sulfide melt that formed pyrrhotite-intermediate solid solution preserved as globules included in phenocryst phases. Stage 2 caused the formation of Cu-rich sulfides by fluid-assisted deposition. The variations of Cu concentrations in available whole-rock analyses from the Sunda arc can be explained by initial concentration in the melt during fractional crystallisation and then extraction by sulfide melt exsolution. Sulfide melt exsolution occurred over a wide compositional range at the arc scale (MgO = 8 – 2.5 wt.%) and resulted in varying degrees of Cu concentration. This behaviour can be modelled by sulfide immiscibility during fractional crystallisation at fO_2 = FMQ +0.8 to +1.4. Higher degrees of Cu enrichment are accompanied by delayed magnetite crystallisation, suggesting an interplay between fO_2, magnetite and Fe-oxide melt saturation and sulfide exsolution. Introduction of a S-O fluid destabilised the sulfide melt (or its crystallised equivalent) and remobilised Cu from both sulfides and the silicate melt. These results indicate that S degassing, which is very active at several volcanoes in the Sunda arc even during periods of quiescence, can transport significant amounts of Cu towards the surface. Mafic-intermediate magmas are thus confirmed as important sources of metals in volcanic arcs, and potential contributors to magmatic-hydrothermal deposits.

Acknowledgements

This research was funded by SIEF (Science and Industry Endowment Fund) and by Post-Doctoral Innovation funds of the NRF (National Research Foundation) of South Africa. Bradley McDonald is thanked for analytical assistance on the LA-ICP-MS.

Figure captions

Figure 1. Satellite images of the Sunda arc, Mt Krakatau and Mt Batur. Au and Au-Cu deposits > 2 Mo indicated by round yellow symbols (Maryono 2015). Structural features from Dahren et al. (2012) and Nishimura and Harjono (1992). Arrows indicate direction of subduction. Image source: Googleearth

Figure 2. **A** Vesicular lava containing sieve-textured plagioclase and clinopyroxene (sample K3, Krakatau, plane polarised transmitted light). **B** Large plagioclase phenocryst with sieve-textured rim and a relatively massive core (sample K2, Krakatau, transmitted plane polarised light). **C** Pyroxene-plagioclase crystal clot (sample B, Batur, transmitted light, crossed polarisers). **D** plagioclase and pyroxene phenocrysts in fine-grained groundmass (sample B, Batur, plane polarised transmitted light). Abbreviations: Cpx clinopyroxene, Pl plagioclase

Figure 3. Whole-rock and melt inclusion compositions of Mt Krakatau and Batur and other volcanoes of the Sunda arc. Data source: http://georoc.mpch-mainz.gwdg.de/; Sutawidjaja et al. (2015). Boundary line between calc-alkaline and tholeiitic series from (Kuno 1968). Melt inclusions: this study. The boundary line between high- and low-FeOT/(FeOT+MgO) groups corresponds to the linear correlation across the analyses

Figure 4. Silicate and sulfide melt inclusions at Mt Krakatau and Batur. **A** Abundant melt inclusions along growth surface in olivine (plane polarised transmitted light, sample B, Batur). **B** Melt inclusion containing partly crystallised glass with multiple bubbles, apatite, and Cu-Fe-sulfide in a bubble (BSE, sample K3, Krakatau). **C** Plagioclase-hosted melt inclusion containing partly crystallised glass with small cavities (bubbles), amphibole, plagioclase crystallised on the inclusion walls and an Cu-Fe-S phase (BSE image, sample K3, Krakatau). Dotted line marks the margin of melt inclusion. Note diffuse boundaries of S-Cu phase. **D** Plagioclase-hosted melt inclusions containing vesicular amphibole, plagioclase and a Cu-Fe-S phase (BSE image, sample B, Batur). **E** Sulfide globule (pyrrhotite-chalcopyrite) co-trapped with melt in plagioclase (sample K2, BSE image). Abbreviations: Am amphibole, Cpx clinopyroxene, Ol olivine, Pl plagioclase, b bubble

Figure 5. Clinopyroxene-hosted melt inclusion containing a large bubble (**A**, **B** BSE images), and X-ray element maps (**C**) showing the presence of Fe-sulfide and Fe-oxide grains precipitated along the bubble walls (sample K3)

Figure 6. Sulfide globule co-trapped with melt in orthopyroxene (**A** and **B**, BSE images) and X-ray compositional maps (**C**). The globule is cracked and O- and Cu-enriched altered domains developed along cracks and along the globule margins, (sample K2, Krakatau). Note the development of effervescence (bubbles) in melt (now glass) close to the sulfide globule. The oxidation was stopped by eruption and quenching of silicate melt to glass, thus preserving evidence of the process. Abbreviations: Po pyrrhotite, Ccp chalcopyrite, Opx orthopyroxene

Figure 7. Composition of sulfide phases. Field of stability of solid solutions at 600°C from (Cabri 1973)

Figure 8. Plots of trace element compositions of melt inclusions from Krakatau and Batur (LA-ICP-MS)

Figure 9. Plot of LA-ICP-MS signal intensity (counts per second, cps) versus time (s) showing the heterogeneous distribution of Cu, due to sulfide phases in melt inclusions. Sample B28_3, Batur, 1664 ppm Cu

Figure 10. Modelling of Cu and S concentrations during fractional crystallisation and sulfide saturation in the Sunda arc compared with whole-rock and glass compositions. MgO as wt.%, Cu and S as ppm. S and Cu contents are modelled at P = 2 kbar and fO_2 = FMQ +0.8 to +1.4, assuming initial S = 1000 ppm. Sulfide solubility model by Mavrogenes and O'Neill (1999). See text for further details. Data sources: see Fig 3

Additional figure 1. Compositions of phenocrysts at Krakatau and Batur. **A** Mg# (=Mg/(Mg+Fe), mol) of pyroxene, **B** Mg# of olivine and **C** anorthite content of plagioclase. Shaded areas indicate calculated phenocryst compositions in equilibrium with basalt and basaltic andesite (grey areas, whole-rock analyses with SiO_2 <55 wt.%), andesite (blue) and dacite-rhyolite (green). Phenocryst composition calculated assuming KD(Fe-Mg) = 0.30 for olivine, 0.27 for pyroxene, and KD(Ca-Na) = 0.27 for plagioclase. Literature data from Dahren et al. (2012); Reubi and Nicholls (2005); Gardner et al. (2013); Camus et al. (1987); Mandeville et al. (1996)

Additional figure 2. Sulfide globules and irregular Fe-oxide inclusions, likely trapped as sulfide and Fe-oxide melts, at Batur and Krakatau. **A** Pyrrhotite-chalcopyrite globule co-trapped with silicate melt, now crystallised. The sulfide globule is partly altered along cracks, indicating sub-solidus alteration (sample K3, Krakatau, plane polarised transmitted and reflected light). **B** Round magnetite grain co-trapped with glass and sulfide globule in orthopyroxene. Magnetite includes pyrrhotite and apatite (sample K3, Krakatau, BSE image). **C** Fe-S-O phase lining a vesicle in microgranular groundmass (sample K3, BSE image). **D** Lobed Fe-oxide inclusions in plagioclase (sample K2, Krakatau, parallel polarised transmitted light). **E** Multiple olivine-hosted, elongate and locally necked (arrowed) Fe-oxide inclusions in contact with glass (sample B, Batur, BSE image). **F** Lobed inclusion of Fe-oxide co-trapped with melt (now crystallised to plagioclase and amphibole) in plagioclase host (sample B, Batur, BSE image)

Additional figure 3. A, **B** Plagioclase-hosted melt inclusion containing amphibole, plagioclase, Cu-S-Fe phase and a small cavity (bubble) (BSE images) and **C** X-ray maps. Sample K2, Krakatau. Abbreviations: Am amphibole, Pl plagioclase, b bubble

References

609 Agustan, Kimata F, Pamitro YE, Abidin HZ (2012) Understanding the 2007–2008 eruption of Anak
610 Krakatau Volcano by combining remote sensing technique and seismic data. International
611 Journal of Applied Earth Observation and Geoinformation 14:73-82. doi:
612 http://dx.doi.org/10.1016/j.jag.2011.08.011.
613 Aiuppa A, Bani P, Moussallam Y, Di Napoli R, Allard P, Gunawan H, Hendrasto M, Tamburello G
614 (2015) First determination of magma-derived gas emissions from Bromo volcano, eastern
615 Java (Indonesia). Journal of Volcanology and Geothermal Research 304:206-213. doi:
616 http://dx.doi.org/10.1016/j.jvolgeores.2015.09.008.
617 Arif J, Baker T (2004) Gold paragenesis and chemistry at Batu Hijau, Indoneisa: implications for gold-
618 rich porphyry copper deposits. Mineralium Deposita 39:523-535. doi: 10.1007/s00126-004-
619 0433-0.
620 Ariskin AA (1996) Calculation of titanomagnetite stability on the liquidus of basalts and andesites
621 with special referenceto tholeiitic magma differentiation. Geochemical International 36:15-
622 23.
623 Audétat A, Pettke T, Heinrich CA, Bodnar RJ (2008) Special paper: The composition of magmatic-
624 hydrothermal fluids in barren and mineralized intrusions. Economic Geology 103:877-908.
625 Bani P, Normier A, Bacri C, Allard P, Gunawan H, Hendrasto M, Surono, Tsanev V (2015) First
626 measurement of the volcanic gas output from Anak Krakatau, Indonesia. Journal of
627 Volcanology and Geothermal Research 302:237-241. doi:
628 http://dx.doi.org/10.1016/j.jvolgeores.2015.07.008.
629 Bell AS, Simon A (2011) Experimental evidence for the alteration of the Fe3+/ΣFe of silicate melt
630 caused by the degassing of chlorine-bearing aqueous volatiles. Geology 39:499-502.
631 Berlo K, van Hinsberg VJ, Vigouroux N, Gagnon JE, Williams-Jones AE (2014) Sulfide breakdown
632 controls metal signature in volcanic gas at Kawah Ijen volcano, Indonesia. Chemical Geology:
633 371, 115-127.
634 Blundy J, Mavrogenes J, Tattitch B, Sparks S, Gilmer A (2015) Generation of porphyry copper
635 deposits by gas-brine reaction in volcanic arcs. Nature Geosci advance online publication.
636 doi: 10.1038/ngeo2351.
637 Borisova A, Toutain J-P, Dubessy J, Pallister J, Zwick A, Salvi S (2014) H_2O–CO_2–S fluid triggering the
638 1991 Mount Pinatubo climactic eruption (Philippines). Bulletin of Volcanology 76:1-9. doi:
639 10.1007/s00445-014-0800-3.
640 Cabri LJ (1973) New data on phase relations in the Cu-Fe-S system. Economic Geology 68:443-454.
641 Camus G, Gourgaud A, Vincent PM (1987) Petrologic evolution of Krakatau (Indonesia): Implications
642 for a future activity. Journal of Volcanology and Geothermal Research 33:299-316. doi:
643 http://dx.doi.org/10.1016/0377-0273(87)90020-5.
644 Candela PA, Holland HD (1986) A mass transfer model for copper and molybdenum in magmatic
645 hydrothermal systems; the origin of porphyry-type ore deposits. Economic Geology 81:1-19.
646 Canil D, Fedortchouk Y (2001) Olivine-liquid partitioning of vanadium and other trace elements, with
647 applications to modern and ancient picrite. The Canadian Mineralogist 39:319-330.
648 Cooke DR, Hollings P, Walshe JL (2005) Giant porphyry deposits: characteristics, distribution, and
649 tectonic controls. Economic Geology 100:801-818.
650 Curray JR, Shor GG, Raitt RW, Henry M (1977) Seismic refraction and reflection studies of crustal
651 structure of the Eastern Sunda and Western Banda Arcs. Journal of Geophysical Research
652 82:2479-2489. doi: 10.1029/JB082i017p02479.
653 Dahren B, Troll V, Andersson U, Chadwick J, Gardner M, Jaxybulatov K, Koulakov I (2012) Magma
654 plumbing beneath Anak Krakatau volcano, Indonesia: evidence for multiple magma storage
655 regions. Contributions to Mineralogy and Petrology 163:631-651. doi: 10.1007/s00410-011-
656 0690-8.
657 Danyushevsky LV, Plechov P (2011) Petrolog3: Integrated software for modeling crystallization
658 processes. Geochem Geophys Geosyst 12:Q07021. doi: 10.1029/2011GC003516.

659 Dare SAS, Barnes S-J, Beaudoin G (2012) Variation in trace element content of magnetite crystallized
660 from a fractionating sulfide liquid, Sudbury, Canada: Implications for provenance
661 discrimination. Geochimica et Cosmochimica Acta 88:27-50. doi:
662 http://dx.doi.org/10.1016/j.gca.2012.04.032.
663 Davidson P, Kamenetsky V, Cooke DR, Frikken P, Hollings P, Ryan C, Van Achterbergh E, Mernagh T,
664 Skarmeta J, Serrano L, Vargas R (2005) Magmatic precursors of hydrothermal fluids at the
665 Río Blanco Cu-Mo deposit, Chile: links to silicate magmas and metal transport. Economic
666 Geology 100:963-978.
667 de Hoog JCM, Mason PRD, van Bergen MJ (2001) Sulfur and chalcophile elements in subduction
668 zones: constraints from a laser ablation ICP-MS study of melt inclusions from Galunggung
669 Volcano, Indonesia. Geochimica et Cosmochimica Acta 65:3147-3164.
670 de Hoog JCM, Hattori KH, Hoblitt RP (2004) Oxidized sulfur-rich mafic magma at Mount Pinatubo,
671 Philippines. Contributions to Mineralogy and Petrology 146:750-761. doi: 10.1007/s00410-
672 003-0532-4.
673 Desborough GA, Anderson AT, Wright TL (1968) Mineralogy of sulfides from certain Hawaiian
674 basalts. Economic Geology 63:636-644.
675 Di Muro A, Pallister J, Villemant B, Newhall C, Semet M, Martinez M, Mariet C (2008) Pre-1991 sulfur
676 transfer between mafic injections and dacite magma in the Mt. Pinatubo reservoir. Journal
677 of Volcanology and Geothermal Research 175:517-540. doi:
678 http://dx.doi.org/10.1016/j.jvolgeores.2008.02.025.
679 Dilles JH, Kent AJR, Wooden JL, Tosdal RM, Koleszar A, Lee RG, Farmer LP (2015) Zircon
680 compositional evidence for sulfur-degassing from ore-forming arc magmas. Economic
681 Geology 110:241-251.
682 Edmonds M, Aiuppa A, Humphreys M, Moretti R, Giudice G, Martin RS, Herd RA, Christopher T
683 (2010) Excess volatiles supplied by mingling of mafic magma at an andesite arc volcano.
684 Geochem Geophys Geosyst 11. doi: 10.1029/2009GC002781.
685 Ewart A, Griffin WL (1994) Application of proton-microprobe data to trace-element partitioning in
686 volcanic rocks. Chemical Geology 117:251-284. doi: http://dx.doi.org/10.1016/0009-
687 2541(94)90131-7.
688 Gardner MF, Troll VR, Gamble JA, Gertisser R, Hart GL, Ellam RM, Harris C, Wolff JA (2013) Crustal
689 Differentiation Processes at Krakatau Volcano, Indonesia. Journal of Petrology 54:149-182.
690 Halter WE, Pettke T, Heinrich CA (2002) The origin of Cu/Au ratios in porphyry-type ore deposits.
691 Science 296:1844-1846.
692 Harjono H, Diament M, Nouaili L, Dubois J (1989) Detection of magma bodies beneath Krakatau
693 volcano (Indonesia) from anomalous shear waves. Journal of Volcanology and Geothermal
694 Research 39:335-348. doi: http://dx.doi.org/10.1016/0377-0273(89)90097-8.
695 Hattori K (1993) High-sulfur magma, a product of fluid discharge from underlying mafic magma:
696 Evidence from Mount Pinatubo, Philippines. Geology 21:1083-1086.
697 Hattori KH, Keith JD (2001) Contribution of mafic melt to porphyry copper mineralization: evidence
698 from Mount Pinatubo, Philippines, and Bingham Canyon, Utah, USA. Mineralium Deposita
699 36:799-806. doi: 10.1007/s001260100209.
700 Hedenquist JW, Lowenstern JB (1994) The role of magmas in the formation of hydrothermal ore
701 deposits. Nature 370:519-527.
702 Heinrich CA, Ryan CG, Mernagh TP, Eadington PJ (1992) Segregation of ore metals between
703 magmatic brine and vapor: a fluid inclusion study using PIXE microanalysis. Economic
704 Geology 87:1566-1583.
705 Hurai V, Simon K, Wiechert U, Hoefs J, Konečný P, Huraiová M, Pironon J, Lipka J (1998) Immiscible
706 separation of metalliferous Fe/Ti-oxide melts from fractionating alkali basalt: P-T-f O2
707 conditions and two-liquid elemental partitioning. Contributions to Mineralogy and Petrology
708 133:12-29. doi: 10.1007/s004100050433.

709 Jaxybulatov K, Koulakov I, Seht MI-v, Klinge K, Reichert C, Dahren B, Troll VR (2011) Evidence for high
710 fluid/melt content beneath Krakatau volcano (Indonesia) from local earthquake
711 tomography. Journal of Volcanology and Geothermal Research 206:96-105. doi:
712 http://dx.doi.org/10.1016/j.jvolgeores.2011.06.009.
713 Jenner FE, O'Neill HSTC, Arculus RJ, Mavrogenes JA (2010) The magnetite crisis in the evolution of
714 arc-related magmas and the initial concentration of Au, Ag and Cu. Journal of Petrology
715 51:2445-2464.
716 Jenner FE, Hauri EH, Bullock ES, König S, Arculus RJ, Mavrogenes JA, Mikkelson N, Goddard C (2015)
717 The competing effects of sulfide saturation versus degassing on the behavior of the
718 chalcophile elements during the differentiation of hydrous melts. Geochem Geophys
719 Geosyst 16:1490-1507. doi: 10.1002/2014GC005670.
720 Jochum KP, Weis U, Stoll B, Kuzmin D, Yang Q, Raczek I, Jacob DE, Stracke A, Birbaum K, Frick DA,
721 Günther D, Enzweiler J (2011) Determination of reference values for NIST SRM 610–617
722 glasses following ISO guidelines. Geostandards and Geoanalytical Research 35:397-429. doi:
723 10.1111/j.1751-908X.2011.00120.x.
724 Jugo PJ, Luth RW, Richards JP (2005) Experimental data on the speciation of sulfur as a function of
725 oxygen fugacity in basaltic melts. Geochimica et Cosmochimica Acta 69:497-503. doi:
726 http://dx.doi.org/10.1016/j.gca.2004.07.011.
727 Kamenetsky VS, Kamenetsky MB (2010) Magmatic fluids immiscible with silicate melts: examples
728 from inclusions in phenocrysts and glasses, and implications for magma evolution and metal
729 transport. Geofluids 10:293-311. doi: 10.1111/j.1468-8123.2009.00272.x.
730 Kamenetsky VS, Maas R, Fonseca ROC, Ballhaus C, Heuser A, Brauns M, Norman MD, Woodhead JD,
731 Rodemann T, Kuzmin DV, Bonatti E (2013) Noble metals potential of sulfide-saturated melts
732 from the subcontinental lithosphere. Geology 41:575-578.
733 Keith JD, Whitney JA, Hattori K, Ballantyne GH, Christiansen EH, Barr DL, Cannan TM, Hook CJ (1997)
734 The role of magmatic sulfides and mafic alkaline magmas in the Bingham and Tintic Mining
735 districts, Utah. Journal of Petrology 38:1679-1690.
736 Kiseeva ES, Wood BJ (2013) A simple model for chalcophile element partitioning between sulphide
737 and silicate liquids with geochemical applications. Earth and Planetary Science Letters 383:
738 68-81.
739 Kress V (1997) Magma mixing as a source for Pinatubo sulphur. Nature 389:591-593.
740 Kuno H (1968) Origin of andesite and its bearing on the Island arc structure. Bulletin Volcanologique
741 32:141-176. doi: 10.1007/BF02596589.
742 Larocque ACL, Stimac JA, Keith JD, Huminicki MAE (2000) Evidence for open-system behavior in
743 immiscible Fe–S–O liquids in silicate magmas: implications for contributions of metals and
744 sulfur to ore-forming fluids. The Canadian Mineralogist 38:1233-1249.
745 Li Y, Audétat A (2012) Partitioning of V, Mn, Co, Ni, Cu, Zn, As, Mo, Ag, Sn, Sb, W, Au, Pb, and Bi
746 between sulfide phases and hydrous basanite melt at upper mantle conditions. Earth and
747 Planetary Science Letters 355–356:327-340. doi:
748 http://dx.doi.org/10.1016/j.epsl.2012.08.008.
749 MacLean WH, Shimazaki H (1976) The partition of Co, Ni, Cu, and Zn between sulfide and silicate
750 liquids. Economic Geology 71:1049-1057.
751 Mandeville CW, Carey S, Sigurdsson H (1996) Magma mixing, fractional crystallization and volatile
752 degassing during the 1883 eruption of Krakatau volcano, Indonesia. Journal of Volcanology
753 and Geothermal Research 74:243-274. doi: http://dx.doi.org/10.1016/S0377-
754 0273(96)00060-1.
755 Mandeville CW, Sasaki A, Saito G, Faure K, King R, Hauri E (1998) Open-system degassing of sulfur
756 from Krakatau 1883 magma. Earth and Planetary Science Letters 160:709-722. doi:
757 http://dx.doi.org/10.1016/S0012-821X(98)00122-8.

758 Marinelli G, Tazieff H (1968) L'Ignimbrite et la Caldera de Batur (Bali, Indonesie). Bulletin
759 Volcanologique 32:89-120. doi: 10.1007/BF02596587.
760 Maryono A (2015) Overview of the tectonic setting and geology of porphyry Cu-Au deposits along
761 the eastern Sunda magmatic arc, Indonesia SEG 2015. Hobart, 27-30 September 2015.
762 Mavrogenes JA, O'Neill HSC (1999) The relative effects of pressure, temperature and oxygen fugacity
763 on the solubility of sulfide in mafic magmas. Geochimica et Cosmochimica Acta 63:1173-
764 1180. doi: http://dx.doi.org/10.1016/S0016-7037(98)00289-0.
765 Naldrett AJ (1969) A portion of the system Fe–S–O between 900 and 1080 °C and its application to
766 sulfide ore magmas. Journal of Petrology 10:171-201.
767 Nelson ST, Montana A (1992) Sieve-textured plagioclase in volcanic rocks produced by rapid
768 decompression. American Mineralogist 77: 1242–1249.
769 Nishimura S, Harjono H, Suparka S (1992) The Krakatau islands: The geotectonic setting. GeoJournal
770 28:87-98. doi: 10.1007/BF00177221.
771 Ōba N, Tomita K, Yamamoto M (1992) An interpretation of the 1883 cataclysmic eruption of
772 Krakatau from geochemical studies on the partial melting of granite. GeoJournal 28:99-108.
773 doi: 10.1007/BF00177222.
774 Pallister JS, Hoblitt RP, Reyes AG (1992) A basalt trigger for the 1991 eruptions of Pinatubo volcano?
775 Nature 356:426-428.
776 Park J-W, Campbell IH, Kim J, Moon J-W (2015) The role of late sulfide saturation in the formation of
777 a Cu- and Au-rich magma: insights from the platinum group element geochemistry of
778 Niuatahi–Motutahi Lavas, Tonga Rear Arc. Journal of Petrology 56:59-81.
779 Patten C, Barnes S-J, Mathez EA, Jenner FE (2013) Partition coefficients of chalcophile elements
780 between sulfide and silicate melts and the early crystallization history of sulfide liquid: LA-
781 ICP-MS analysis of MORB sulfide droplets. Chemical Geology 358:170-188. doi:
782 http://dx.doi.org/10.1016/j.chemgeo.2013.08.040.
783 Pichavant M, Macdonald R (2007) Crystallization of primitive basaltic magmas at crustal pressures
784 and genesis of the calc-alkaline igneous suite: experimental evidence from St Vincent, Lesser
785 Antilles arc. Contributions to Mineralogy and Petrology 154: 535-558. <10.1007/s00410-007-
786 0208-6>.
787 Pokrovski GS, Kokh MA, Guillaume D, Borisova AY, Gisquet P, Hazemann J-L, Lahera E, Del Net W,
788 Proux O, Testemale D, Haigis V, Jonchière R, Seitsonen AP, Ferlat G, Vuilleumier R, Saitta AM,
789 Boiron M-C, Dubessy J (2015) Sulfur radical species form gold deposits on Earth. Proceedings
790 of the National Academy of Sciences 112:13484-13489.
791 Prichard HM, Hutchinson D, Fisher PC (2004) Petrology and crystallization history of multiphase
792 sulfide droplets in a mafic dike from Uruguay: Implications for the origin of Cu-Ni-PGE sulfide
793 deposits. Economic Geology 99:365-376.
794 Putirka KD (2008) Thermometers and barometers for volcanic systems. Reviews in Mineralogy and
795 Geochemistry 69:61-120.
796 Reubi O, Nicholls IA (2004a) Magmatic evolution at Batur volcanic field, Bali, Indonesia: petrological
797 evidence for polybaric fractional crystallization and implications for caldera-forming
798 eruptions. Journal of Volcanology and Geothermal Research 138:345-369. doi:
799 http://dx.doi.org/10.1016/j.jvolgeores.2004.07.009.
800 Reubi O, Nicholls IA (2004b) Variability in eruptive dynamics associated with caldera collapse: An
801 example from two successive eruptions at Batur volcanic field, Bali, Indonesia. Bulletin of
802 Volcanology 66:134-148. doi: 10.1007/s00445-003-0298-6.
803 Reubi O, Nicholls IA (2005) Structure and dynamics of a silicic magmatic system associated with
804 caldera-forming eruptions at Batur Volcanic Field, Bali, Indonesia. Journal of Petrology
805 46:1367-1391.
806 Richards JP (2013) Giant ore deposits formed by optimal alignments and combinations of geological
807 processes. Nature Geosci 6:911-916. doi: 10.1038/ngeo1920.

Richards JP (2015) The oxidation state, and sulfur and Cu contents of arc magmas: implications for metallogeny. Lithos 233:27-45. doi: http://dx.doi.org/10.1016/j.lithos.2014.12.011.
Ripley EM, Brophy JG, Li C (2002) Copper solubility in a basaltic melt and sulfide liquid/silicate melt partition coefficients of Cu and Fe. Geochimica et Cosmochimica Acta 66:2791-2800. doi: http://dx.doi.org/10.1016/S0016-7037(02)00872-4.
Self S, King AJ (1996) Petrology and sulfur and chlorine emissions of the 1963 eruption of Gunung Agung, Bali, Indonesia. Bulletin of Volcanology 58:263-285. doi: 10.1007/s004450050139.
Shinohara H (2008) Excess degassing from volcanoes and its role on eruptive and intrusive activity. Rev Geophys 46: 10.1029/2007RG000244.
Sillitoe RH (2010) Porphyry copper systems. Economic Geology 105:3-41.
Simon AC, Ripley EM (2011) The role of magmatic sulfur in the formation of ore deposits. Reviews in Mineralogy and Geochemistry 73:513-578.
Sun W, Arculus RJ, Kamenetsky VS, Binns RA (2004) Release of gold-bearing fluids in convergent margin magmas prompted by magnetite crystallization. Nature 431:975-978. doi: http://www.nature.com/nature/journal/v431/n7011/suppinfo/nature02972_S1.html.
Sutawidjaja IS (1990) Batur berita berkala vulkanologi. Volcanology Survey Indonesia.
Sutawidjaja IS (2009) Ignimbrite analyses of Batur Caldera, Bali, based on ^{14}C dating. Indonesian Journal on Geoscience; Vol 4, No 3 (2009).
Sutawidjaja IS, Rosana MF, Watanabe K (2015) Magma chamber model of Batur Caldera, Bali, Indonesia: Compositional variation of two facies, large-volume dacitic ignimbrites. Indonesian Journal on Geoscience; Vol 2, No 2 (2015).
Tomkins AG, Rebryna KC, Weinberg RF, Schaefer BF (2012) Magmatic sulfide formation by reduction of oxidized arc basalt. Journal of Petrology 53:1537-1567.
Van Hoose AE, Streck MJ, Pallister JS, Wälle M (2013) Sulfur evolution of the 1991 Pinatubo magmas based on apatite. Journal of Volcanology and Geothermal Research 257:72-89. doi: http://dx.doi.org/10.1016/j.jvolgeores.2013.03.007.
Wallace PJ (2001) Volcanic SO_2 emissions and the abundance and distribution of exsolved gas in magma bodies. Journal of Volcanology and Geothermal Research 108:85-106.
Watanabe K, Yamanaka T, Harijoko A, Saitra C, Warmada IW (2010) Caldera activities in north Bali, Indonesia. Journal of SE Asian Applied Geology 2:283-290.
Wheller GE, Varne R (1986) Genesis of dacitic magmatism at Batur volcano, Bali, Indonesia: Implications for the origins of stratovolcano calderas. Journal of Volcanology and Geothermal Research 28:363-378. doi: http://dx.doi.org/10.1016/0377-0273(86)90031-4.
Wilkinson JJ (2013) Triggers for the formation of porphyry ore deposits in magmatic arcs. Nature Geosci 6:917-925. doi: 10.1038/ngeo1940.
Williams-Jones AE, Heinrich CA (2005) 100th anniversary special paper: Vapor transport of metals and the formation of magmatic-hydrothermal ore deposits. Economic Geology 100:1287-1312.
Zajacz Z, Halter W (2009) Copper transport by high temperature, sulfur-rich magmatic vapor: Evidence from silicate melt and vapor inclusions in a basaltic andesite from the Villarrica volcano (Chile). Earth and Planetary Science Letters 282:115-121. doi: http://dx.doi.org/10.1016/j.epsl.2009.03.006.

Table1

Click here to download Table: Table_1.pdf

Table 1. Pressure and temperature estimates at Mt Krakatau and Batur

reference	mineral	depth (pressure)	temperature, °C	method
Mt Krakatau				
Dahren et al., 2012	clinopyroxene	7-12 km, minor to 22 km	1090-1150	
this study	clinopyroxene	up to 22 km (0 - 5.3 kbar)	986-1114	Cpx-liq, Putirka 2008
this study	orthopyroxene	up to 16 km (0 - 4 kbar)	1069-1105	Opx-liq, Putirka 2008
Dahren et al., 2012	plagioclase An56-76, An77-88	3-7 km, 23-28 km	1040-1080, 1100-1190	Pl-liq, Putirka 2008
Mandeville et al., 1996	plagioclase (1883 eruption, felsic-intermediate)	4-8 km (1 - 2 kbar)	880-1000	
this study	plagioclase An>64	12 - 18 km (3.1 - 4.5 kbar)	1123-1134	Pl-liq, Putirka 2008
this study	plagioclase An<64	up to 8 km (0 - 2 kbar)	980-1008	Pl-liq, Putirka 2008
Dahren et al., 2012	olivine		1070-1100	
Mt Batur				
Reubi and Nichols, 2004	2 pyroxenes (basalt, andesite)		1010-1150	2-pyroxene
Reubi and Nichols, 2004	2 pyroxenes (dacite)		990	2-pyroxene
this study	clinopyroxene Mg#>64	up to 22 km (0 - 5.4 kbar)	990-1096	Cpx-liq, Putirka 2008
Reubi and Nichols, 2004	Ol-Pl-Cpx	8-28 km (2 - 7 kbar), <4 km (<1 kbar)		mineral stability
this study	plagioclase An>64	26 - 32 km (6.8 - 8.1 kbar)	1145-1153	Pl-liq, Putirka 2008
this study	plagioclase An<64	up to 8 km (0 - 2.1 kbar)	950-970	Pl-liq, Putirka 2008
this study	olivine		1114-1173	Ol-liq, Purtika 2007

AdditionalTable

Click here to download Table: AdditionalTable_MI_analyses_b.pdf

Additional Table. Melt inclusion analyses (LA-ICP-MS)

Analysis	B_2 - 1	B_2 - 2	B_4 - 1	B_4 - 3	B_74 - 1	B_74 - 2	B_101 - 2	B_58 - 1	B_28 - 1
Host	Ol	Ol	Ol	Ol	Ol	Ol	Ol	Ol	Pl
Prop	0.33	0.08	0.64	0.66	0.20	1.00	0.89	0.45	0.27
Na2O	4.21	4.65	4.06	4.31	4.23	4.30	4.99	3.98	4.86
MgO	7.07	5.02	2.43	0.53	7.93	3.49	0.81	1.04	1.99
Al2O3	17.83	17.53	16.77	18.13	17.87	18.12	16.36	16.78	18.10
SiO2	50.58	56.01	60.99	59.41	48.93	56.93	64.50	60.06	61.23
FeO	9.94	7.54	5.77	6.72	10.25	5.86	3.68	7.39	5.06
P2O5	0.31	0.46	0.34	0.39	0.34	0.34	0.50	0.42	0.26
S	0.28	0.49	0.00	0.04	0.34	0.07	0.05	0.06	0.03
K2O	1.32	1.26	1.70	1.77	1.73	1.72	2.48	1.91	2.04
CaO	7.36	6.42	7.04	7.67	7.67	7.99	5.37	7.37	5.76
TiO2	1.09	0.62	0.92	1.02	0.70	1.19	1.27	1.00	0.67
tot	100	100	100	100	100	100	100	100	100
V	553.3	-	162.2	179.7	180.4	231.6	158.3	245.2	219.2
Mn	1322	956.6	347.0	504.5	1501.8	925.3	483.2	340.7	1396.3
Co	11.31	-	3.31	9.55	33.36	20.27	6.90	-	20.16
Ni	-	7.54	0.86	2.89	-	19.97	3.50	-	<13.53
Cu	177.0	221.7	140.2	120.8	987.2	118.5	180.9	76.3	2559.8
Zn	73.94		49.79	60.23	119.73	75.20	38.94	35.09	94.03
As	6.97	40.47	<2.66	<3.03	6.62	2.77	2.13	4.40	-
Rb	19.73	19.55	23.34	25.72	25.89	21.56	29.76	32.48	30.19
Sr	418.7	468.8	238.3	286.3	341.5	252.1	201.1	225.9	620.5
Y	27.8	35.2	18.1	21.7	22.1	21.6	20.9	25.0	21.9
Zr	69.0	82.6	70.1	79.4	61.8	69.8	80.3	106.4	73.0
Nb	3.87	4.23	3.50	4.19	2.03	4.46	4.86	6.12	4.52
Mo	0.55	<1.62	<2.75	<3.80	1.12	0.79	0.90	0.79	0.54
Ag	0.07	<0.03	0.07	<0.06	0.28	0.08	0.08	0.03	0.11
Sn	-	<1.95	<3.32	0.61	1.48	0.92	1.02	0.99	1.13
Sb	2.02	12.26	0.33	<0.22	1.98	0.09	0.23	0.36	0.51
Ba	241.4	217.6	204.5	240.7	260.8	218.9	236.9	276.2	434.4
La	10.13	2.69	10.11	11.92	10.93	11.64	12.81	13.98	15.71
Ce	25.3	13.2	22.1	25.3	20.4	25.1	27.1	29.3	30.9
Pr	na	na	na	na	na	na	na	na	na
Nd	na	na	na	na	na	na	na	na	na
Sm	na	na	na	na	na	na	na	na	na
Eu	na	na	na	na	na	na	na	na	na
Gd	4.68	<3.12	<5.30	<7.32	3.16	3.90	<4.58	<6.89	3.49
Dy	4.46	5.51	3.59	<4.52	3.94	3.68	4.20	<4.28	3.30
Er	na	na	na	na	na	na	na	na	na
Tm	na	na	na	na	na	na	na	na	na
Yb	5.08	<2.24	2.30	<5.25	2.87	2.57	<3.29	3.00	<4.55
Lu	na	na	na	na	na	na	na	na	na
Pb	10.23	1.63	4.06	6.08	95.17	4.96	5.58	5.77	8.95
Th	2.00	1.99	2.16	2.54	0.82	2.13	2.44	3.01	1.97

Major element oxides as wt.%, trace elements as ppm

x mass proportion between the inclusion and the ablated volume

Analysis	B_28 - 3	B_44 - 3	B_34 - 2	B_21 - 1	K2_27 - 3	K2_32 - 1 - 1	K2_43 - 1	K2_46 - 1	K2_46 - 2
Host	Pl	Pl	Pl	Pl	Pl	Pl	Cpx	Cpx	Cpx
Prop	0.67	0.64	0.55	0.85	0.62	0.54	0.37	0.75	0.16
Na2O	4.50	4.08	4.33	3.43	4.12	4.69	5.52	3.97	2.72
MgO	1.49	3.19	2.07	2.83	2.67	1.20	1.35	3.27	10.25
Al2O3	18.08	18.14	18.10	18.14	18.11	18.05	18.02	18.05	14.91
SiO2	62.96	56.23	60.61	56.15	58.15	64.26	65.30	61.16	50.48
FeO	3.99	6.98	5.15	6.91	5.45	2.75	0.84	2.57	8.32
P2O5	0.13	0.26	0.17	0.90	0.43	0.17	0.70	0.37	0.12
S	0.06	0.09	0.04	0.03	0.10	0.26	0.06	0.05	0.11
K2O	1.79	1.40	1.46	1.39	1.22	2.30	1.33	1.13	0.27
CaO	6.60	8.62	7.45	9.04	8.73	5.72	6.23	8.79	12.21
TiO2	0.39	1.01	0.61	1.17	1.02	0.61	0.64	0.63	0.60
tot	100	100	100	100	100	100	100	100	100
V	136.8	396.1	229.1	260.1	235.4	62.9	53.8	107.0	243.6
Mn	1227.5	2064	1668.3	2699	1940.6	1152.0	356.4	737.0	1620.8
Co	16.44	30.47	23.13	35.30	27.50	6.71	-	8.95	17.71
Ni	<13.96	5.78	5.14	9.09	39.78	1.79	<6.24	7.69	16.47
Cu	1664.2	1330.3	547.7	1631.9	6731.3	88.9	146.3	26.1	14.4
Zn	89.93	139.68	111.77	175.20	153.72	60.08	26.01	36.96	76.25
As	7.28	5.30	17.25	17.30	1.97	37.48	5.30	3.73	0.49
Rb	39.56	33.99	46.34	60.68	34.62	77.04	30.22	25.62	4.48
Sr	629.5	593.6	634.6	568.6	483.3	446.5	338.6	324.1	322.1
Y	14.5	35.0	22.4	100.5	42.7	68.6	49.7	24.3	8.9
Zr	49.2	119.2	76.6	432.8	135.3	441.2	162.4	101.7	23.6
Nb	2.82	6.03	3.50	25.39	4.21	10.03	4.00	2.92	0.67
Mo	0.59	<2.48	0.81	3.00	<2.34	2.18	<1.56	<1.74	<1.41
Ag	0.21	0.13	0.05	0.35	1.18	0.15	0.10	0.04	<0.01
Sn	0.86	1.41	1.15	2.83	1.54	1.99	0.36	0.67	0.23
Sb	0.56	0.27	2.17	1.96	0.08	12.94	0.32	0.65	0.51
Ba	409.2	333.0	330.8	402.3	187.8	399.6	233.9	168.3	63.5
La	13.56	18.89	14.49	43.10	16.97	30.62	23.20	13.91	4.40
Ce	25.5	40.8	29.9	98.6	42.4	73.5	62.0	32.8	12.4
Pr	na	na	na	na	na	na	na	na	na
Nd	na	na	na	na	na	na	na	na	na
Sm	na	na	na	na	na	na	na	na	na
Eu	na	na	na	na	na	na	na	na	na
Gd	<6.52	<4.77	4.56	16.54	4.20	10.86	10.37	4.82	2.07
Dy	2.80	3.77	<5.24	16.17	5.08	11.32	7.41	4.53	2.17
Er	na	na	na	na	na	na	na	na	na
Tm	na	na	na	na	na	na	na	na	na
Yb	<4.69	<3.43	<6.07	10.20	<3.03	2.86	6.13	2.40	1.12
Lu	na	na	na	na	na	na	na	na	na
Pb	8.31	9.91	9.62	12.35	11.99	15.99	8.53	5.06	3.80
Th	1.52	3.60	2.22	13.82	3.57	13.04	3.97	2.86	0.59

Analysis	K2_48 - 2	K3_17 - 1	K3_49 - 1	K3_8 - 1	K3_14 - 1	K3_14 - 4	K3_9 - 1	K3_5 - 1	K3_5 - 1
Host	Cpx	Pl	Cpx	Pl	Pl	Pl	Pl	Pl	Pl
Prop	0.83	0.35	0.20	0.58	0.41	0.45	1.00	0.63	0.61
Na2O	5.47	5.37	4.16	5.14	6.02	5.08	3.75	4.28	4.25
MgO	2.46	0.97	3.60	2.00	1.55	1.36	2.63	3.10	3.09
Al2O3	17.18	18.04	18.11	18.12	18.08	18.07	18.13	18.13	18.13
SiO2	63.06	66.74	57.37	59.78	63.28	64.77	57.29	58.73	58.71
FeO	1.99	2.22	5.61	5.88	3.95	3.69	6.70	6.37	6.40
P2O5	0.43	0.12	0.46	0.33	0.25	0.26	0.45	0.15	0.15
S	0.14	0.02	0.10	0.22	0.07	0.00	0.28	0.10	0.10
K2O	4.22	0.99	1.51	1.34	1.93	1.55	1.30	1.49	1.45
CaO	4.39	5.25	8.01	6.34	4.31	4.71	8.42	6.86	6.93
TiO2	0.66	0.28	1.07	0.86	0.58	0.52	1.04	0.80	0.79
tot	100	100	100	100	100	100	100	100	100
V	77.6	24.2	121.3	175.0	56.5	67.2	374.0	334.5	329.2
Mn	822.9	579.6	1352.6	1429.5	1172.0	1005.6	2644	1801.0	1777.6
Co	4.58	6.77	1.36	16.80	14.21	12.09	36.78	22.70	22.29
Ni	1.50	1.97	4.04	3.97	3.74	4.99	<14.95	5.25	5.63
Cu	350.2	8.7	403.7	104.5	174.0	206.9	294.8	619.9	647.2
Zn	36.63	47.37	158.08	74.86	98.23	65.91	149.13	139.62	135.37
As	29.49	46.14	9.01	26.20	7.98	29.77	45.27	6.75	6.20
Rb	71.72	29.47	34.20	34.60	61.65	45.61	60.28	25.57	24.69
Sr	279.8	659.9	281.5	614.8	438.3	507.7	556.8	457.6	459.3
Y	30.0	21.2	36.4	38.5	46.4	33.5	68.5	26.2	25.5
Zr	134.0	119.8	178.2	162.3	240.8	178.3	301.6	60.3	59.5
Nb	3.97	3.46	2.50	3.77	7.20	5.44	10.90	1.86	1.82
Mo	0.77	<4.34	<1.60	0.68	1.37	1.13	2.00	<2.10	<2.07
Ag	0.29	<0.06	0.15	<0.05	0.07	0.09	0.51	0.12	0.11
Sn	<2.39	1.34	2.54	<3.23	2.05	-	<4.28	1.12	1.14
Sb	11.12	10.59	0.11	7.97	0.35	5.17	11.76	0.74	0.66
Ba	237.1	185.1	242.4	302.6	330.1	249.3	409.7	207.6	198.8
La	18.08	11.49	48.30	22.31	23.44	18.39	37.92	11.28	11.18
Ce	41.5	26.6	95.2	50.7	54.4	42.9	93.7	27.7	27.2
Pr	na	na	na	na	na	na	na	na	na
Nd	na	na	na	na	na	na	na	na	na
Sm	na	na	na	na	na	na	na	na	na
Eu	na	na	na	na	na	na	na	na	na
Gd	3.46	<7.96	6.11	<5.16	7.80	<5.89	<6.81	<4.02	<3.98
Dy	5.48	<4.96	7.42	6.68	8.85	6.18	15.13	1.44	1.27
Er	na	na	na	na	na	na	na	na	na
Tm	na	na	na	na	na	na	na	na	na
Yb	1.99	2.01	4.35	4.16	<3.38	4.06	8.76	2.59	2.72
Lu	na	na	na	na	na	na	na	na	na
Pb	8.91	5.46	33.39	8.53	12.39	10.58	13.54	9.60	9.60
Th	3.79	2.35	5.14	4.29	6.94	5.17	7.91	1.26	1.24

Analysis	K3_5 - 2	B_Ol - 1	B_Ol - 5	B_Ol - 12	B_Pl_2 - 1	B_Pl - 3	B_Pl - 5	K3_Pl - 2
Host	Pl	Ol	Ol	Ol	Pl	Pl	Pl	Pl
Prop	0.67	0.89	0.68	0.90	0.25	0.30	1.05	0.41
Na2O	4.57	4.33	4.17	4.02	3.09	4.95	4.03	4.97
MgO	3.45	4.55	5.05	5.75	1.48	2.93	2.86	1.46
Al2O3	18.13	18.31	18.30	18.29	28.44	19.59	18.37	22.72
SiO2	58.16	56.81	56.91	55.73	55.62	56.21	56.10	62.66
FeO	6.62	6.56	6.49	6.38	3.75	7.00	7.86	3.07
P2O5	0.21	0.30	0.31	0.27	0.04	0.29	0.30	0.22
S	0.08	0.08	0.08	0.09	0.34	0.20	0.04	0.16
K2O	1.27	1.70	1.55	1.65	0.53	3.37	1.91	1.53
CaO	6.59	6.36	6.29	6.86	6.22	4.61	7.63	2.69
TiO2	0.93	1.01	0.85	0.96	0.49	0.85	0.90	0.52
tot	100	100.00	100.00	100.00	100.00	100.00	100.00	100.00
V	361.7	301.46	306.91	279.26	153.46	146.70	263.64	48.13
Mn	1812.3	1382.27	1337.58	1339.43	782.87	1693.58	1586.04	680.20
Co	24.95	29.91	20.14	36.63	11.66	21.93	20.14	8.62
Ni	3.62	15.42	4.93	28.14	<0.67	4.10	3.13	1.07
Cu	204.5	156.88	192.26	127.97	294.91	1299.07	1612.28	73.42
Zn	130.62	130.67	153.14	132.09	65.88	174.43	137.43	55.62
As	6.81	0.00	0.00	0.00	0.00	0.00	0.00	0.00
Rb	29.91	30.70	27.00	25.41	10.36	65.73	34.04	32.70
Sr	480.6	356.92	386.66	333.73	296.76	95.49	346.19	0.62
Y	35.1	29.48	28.16	25.95	16.06	34.10	29.60	23.11
Zr	97.0	103.65	88.42	89.41	63.24	194.68	107.36	115.12
Nb	2.07	5.83	4.84	4.95	1.16	10.11	6.25	3.20
Mo	0.58	<5.14	1.00	<3.45	<5.54	1.39	1.09	<4.53
Ag	0.09	0.13	0.13	0.10	<0.18	<0.10	0.23	<0.06
Sn	1.63	1.64	1.70	1.37	1.46	2.17	1.85	1.49
Sb	0.67	na	na	na	na	na	na	na
Ba	230.6	na	na	na	na	na	na	na
La	15.34	16.14	14.00	13.53	8.08	21.74	18.96	11.88
Ce	36.1	35.23	29.53	29.24	18.37	45.99	40.84	28.91
Pr		4.38	3.61	3.54	2.33	5.44	5.02	3.68
Nd		21.31	17.69	18.39	4.27	20.72	24.69	14.53
Sm		5.59	3.68	4.76	3.42	3.17	6.75	4.57
Eu		1.56	1.32	1.45	<1.30	2.34	1.81	0.67
Gd	6.74	6.03	4.57	5.13	<4.66	<3.49	6.54	4.93
Dy	6.28	6.11	5.48	5.63	<2.86	2.45	6.31	<2.28
Er		3.84	3.59	3.29	1.95	<1.63	3.87	2.85
Tm		<0.59	<0.42	0.43	<0.64	<0.48	0.50	<0.51
Yb	<3.10	3.71	3.07	3.04	1.91	4.51	3.82	<2.74
Lu		<0.67	0.48	0.45	<0.72	0.60	<0.52	0.41
Pb	7.46	7.43	6.73	6.25	4.55	14.26	9.35	6.79
Th	2.28	na	na	na	na	na	na	na

Analysis	K3_Pl - 11	K3_Pl - 23	K2_Pl - 13	K2_Pl - 20	K2_Pl - 25
Host	Pl	Pl	Pl	Pl	Pl
Prop	0.58	0.40	0.25	0.29	0.75
Na2O	5.99	5.29	3.67	5.92	6.29
MgO	2.03	1.29	1.51	0.88	0.89
Al2O3	18.19	23.48	18.16	18.10	18.13
SiO2	63.18	61.30	60.32	67.91	63.97
FeO	4.04	2.51	4.07	2.38	2.78
P2O5	0.39	0.09	0.36	0.18	0.15
S	0.08	0.10	0.20	0.15	0.05
K2O	1.73	1.08	1.24	1.77	2.64
CaO	3.64	4.50	9.80	2.20	4.71
TiO2	0.73	0.35	0.65	0.50	0.39
tot	100.00	100.00	100.00	100.00	100.00
V	86.84	25.00	76.15	39.79	36.45
Mn	934.88	588.05	1025.83	819.79	860.27
Co	10.90	7.723	10.97	2.65	3.38
Ni	2.28	2.41	1.348	0.72	2.02
Cu	211.12	218.15	162.69	181.36	100.81
Zn	76.15	52.07	68.87	65.59	52.54
As	0.00	0.00	0.00	0.00	0.00
Rb	31.77	19.20	27.43	72.04	43.47
Sr	267.92	162.13	226.26	178.98	242.20
Y	29.71	22.68	33.00	40.46	29.67
Zr	128.34	110.36	134.02	195.81	112.09
Nb	3.85	3.34	3.59	4.68	3.25
Mo	<4.14	<4.10	<6.48	1.02	<4.92
Ag	<0.05	0.17	<0.07	0.14	0.03
Sn	1.55	1.70	1.81	2.41	2.09
Sb	na	na	na	na	na
Ba	na	na	na	na	na
La	15.91	13.23	15.19	19.63	17.87
Ce	37.72	30.71	35.96	46.18	38.91
Pr	5.01	3.87	4.39	5.83	4.80
Nd	23.64	18.72	<5.04	29.66	21.81
Sm	3.20	4.54	6.24	<5.46	5.80
Eu	1.37	<3.29	<1.41	<1.48	1.17
Gd	3.65	<2.01	<5.04	<5.29	5.43
Dy	4.43	<1.53	<3.08	<3.23	5.48
Er	2.66	<0.45	<2.33	<2.45	3.42
Tm	<0.46	<2.41	<0.69	<0.72	<0.50
Yb	<2.47	<0.51	<3.69	<3.87	<2.71
Lu	<0.52	<1.06	<0.78	<0.82	<0.57
Pb	7.83	7.64	5.15	12.18	4.78
Th	na	na	na	na	na

Figure1

Click here to download high resolution image

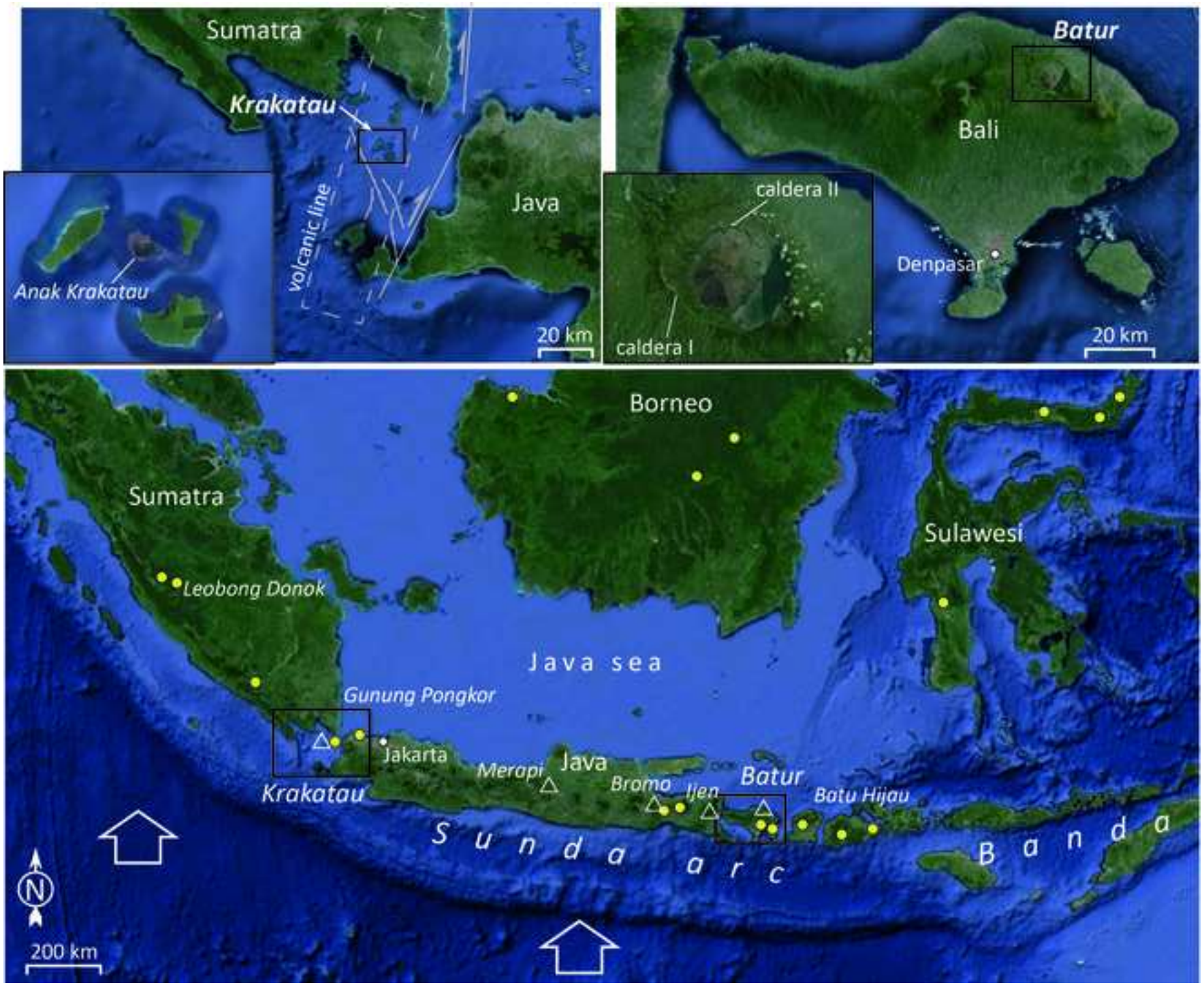

Figure2

Click here to download high resolution image

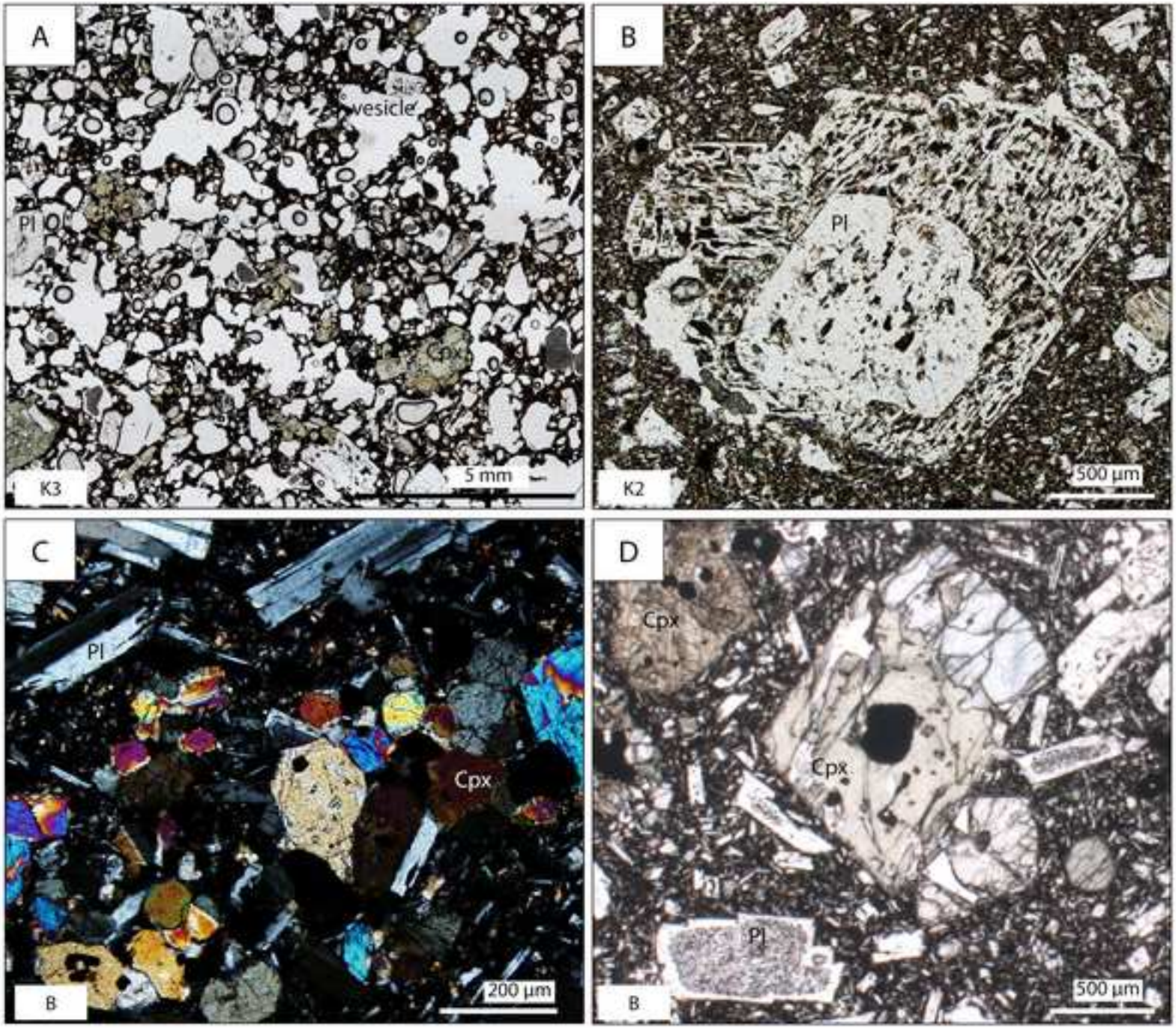

Figure3

Click here to download Figure: Fig3_review.eps

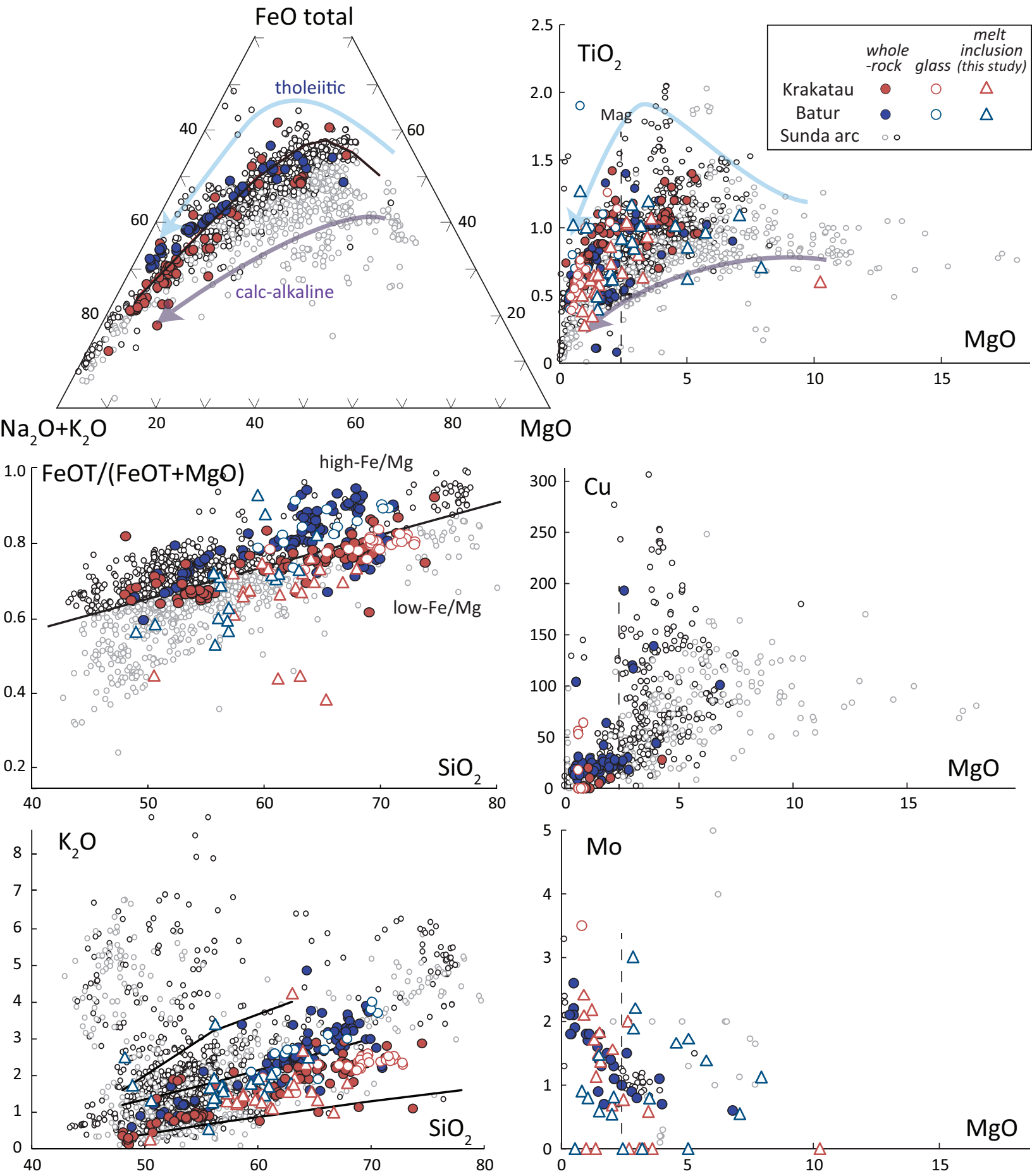

Figure4

Click here to download high resolution image

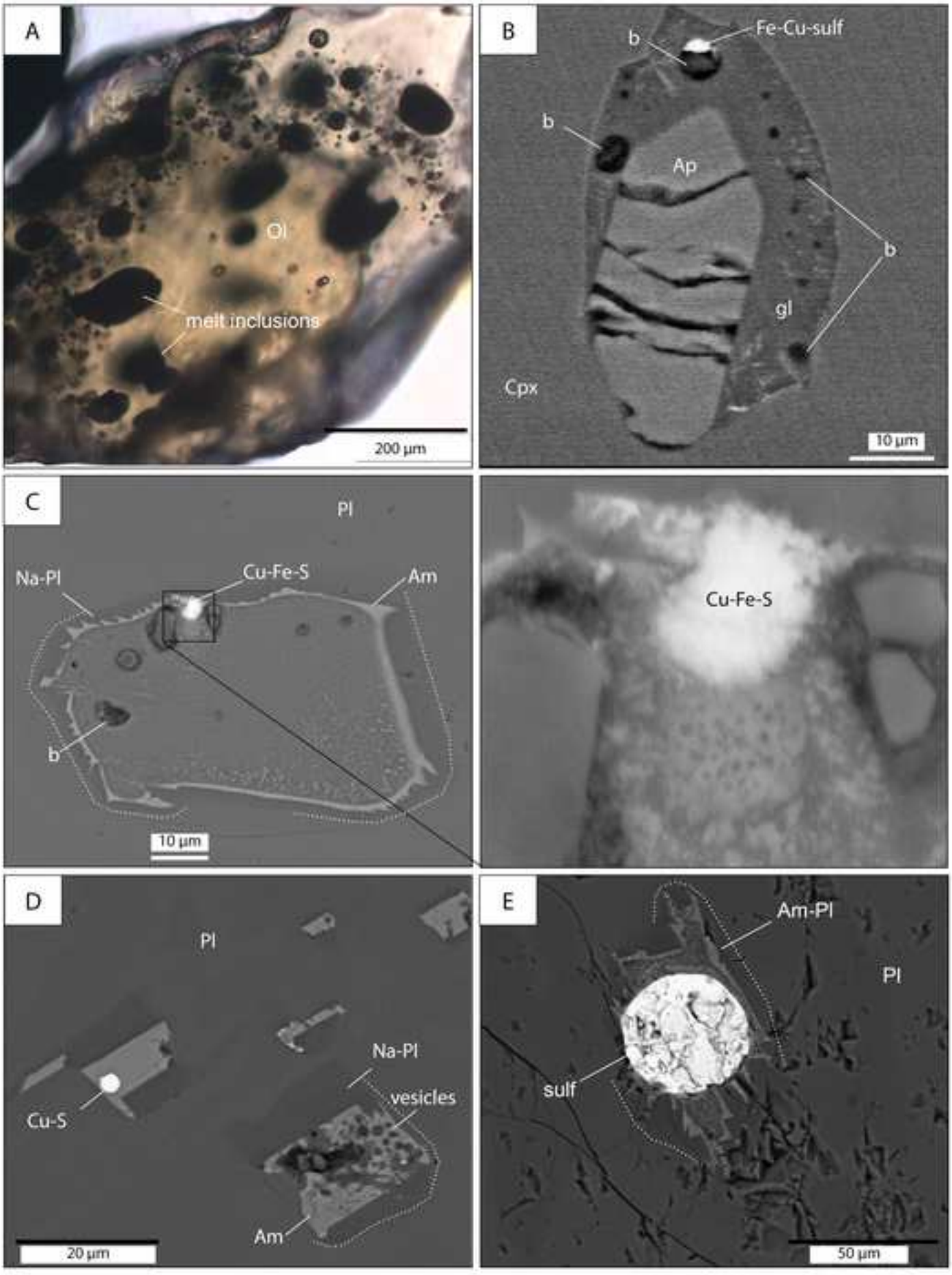

Figure5

Click here to download high resolution image

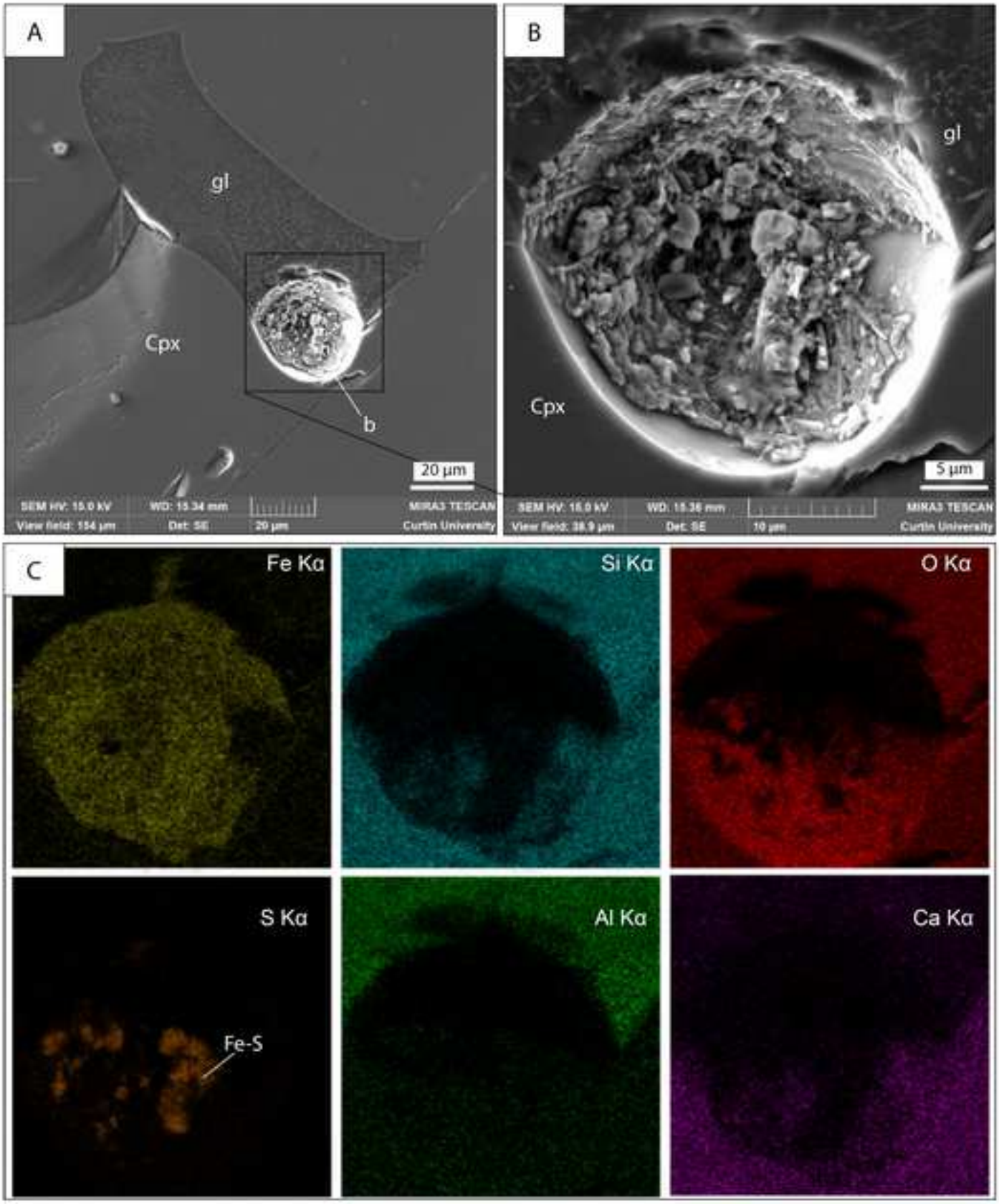

Figure6

Click here to download high resolution image

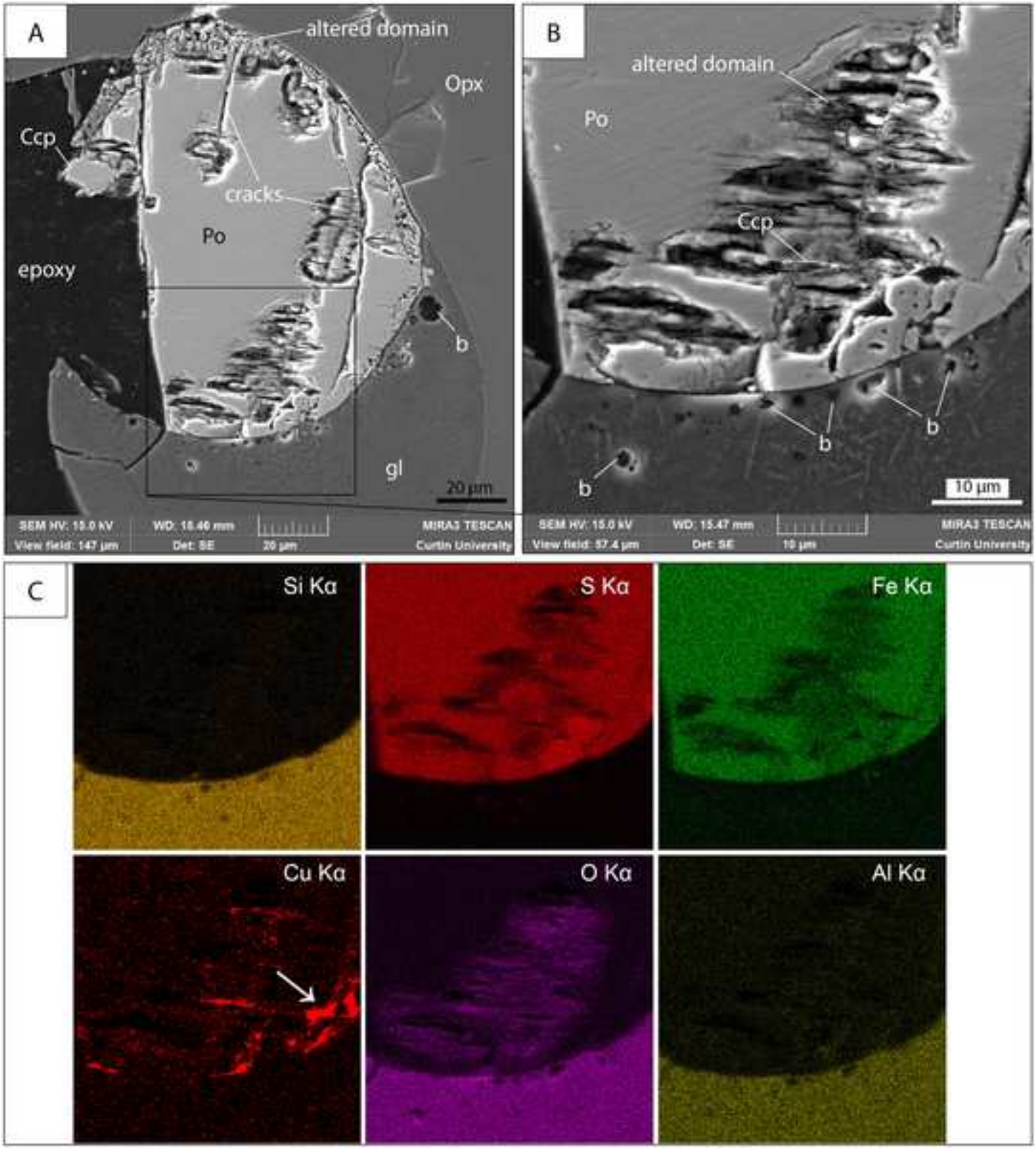

Figure7
Click here to download Figure: Fig7_review.eps

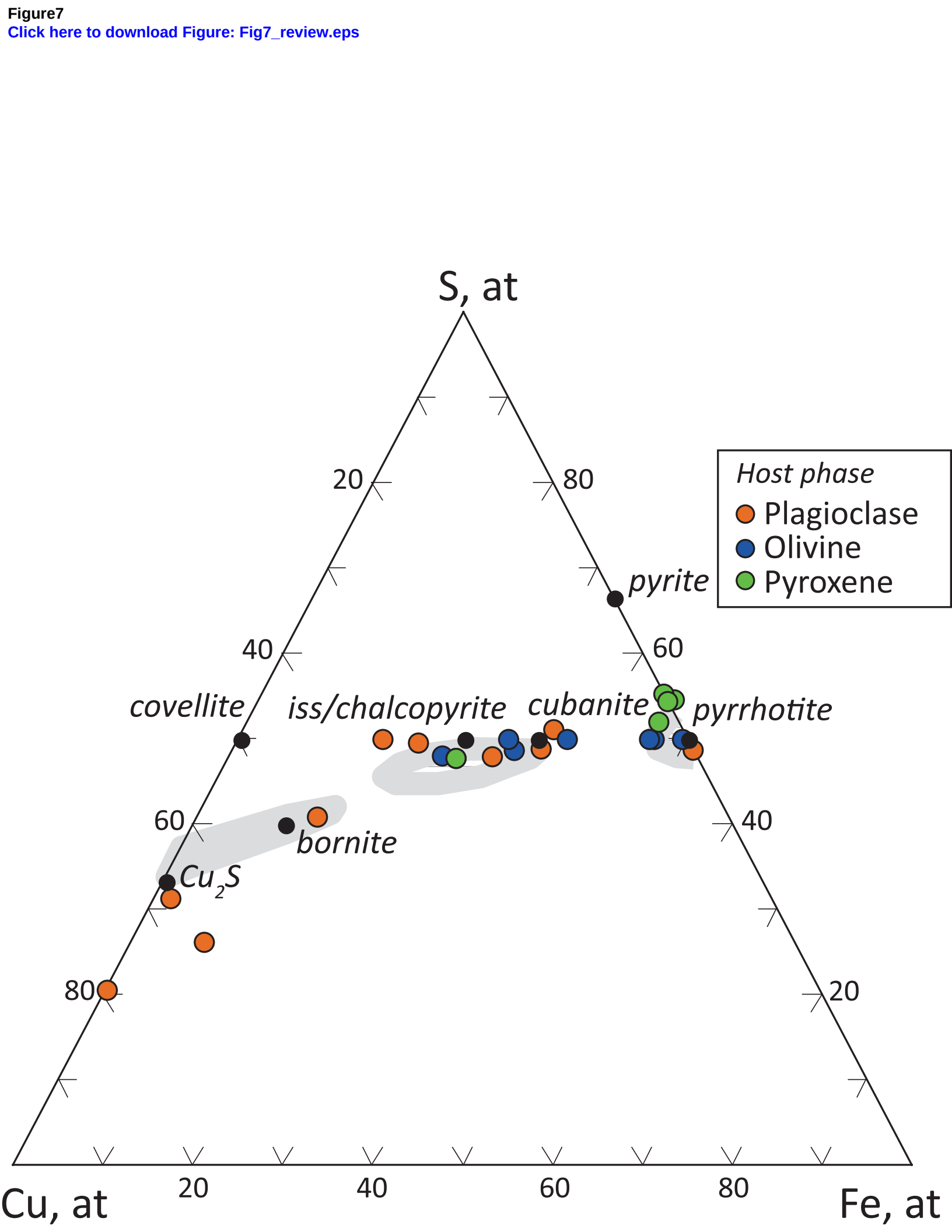

Figure8

Click here to download Figure: Fig8.eps

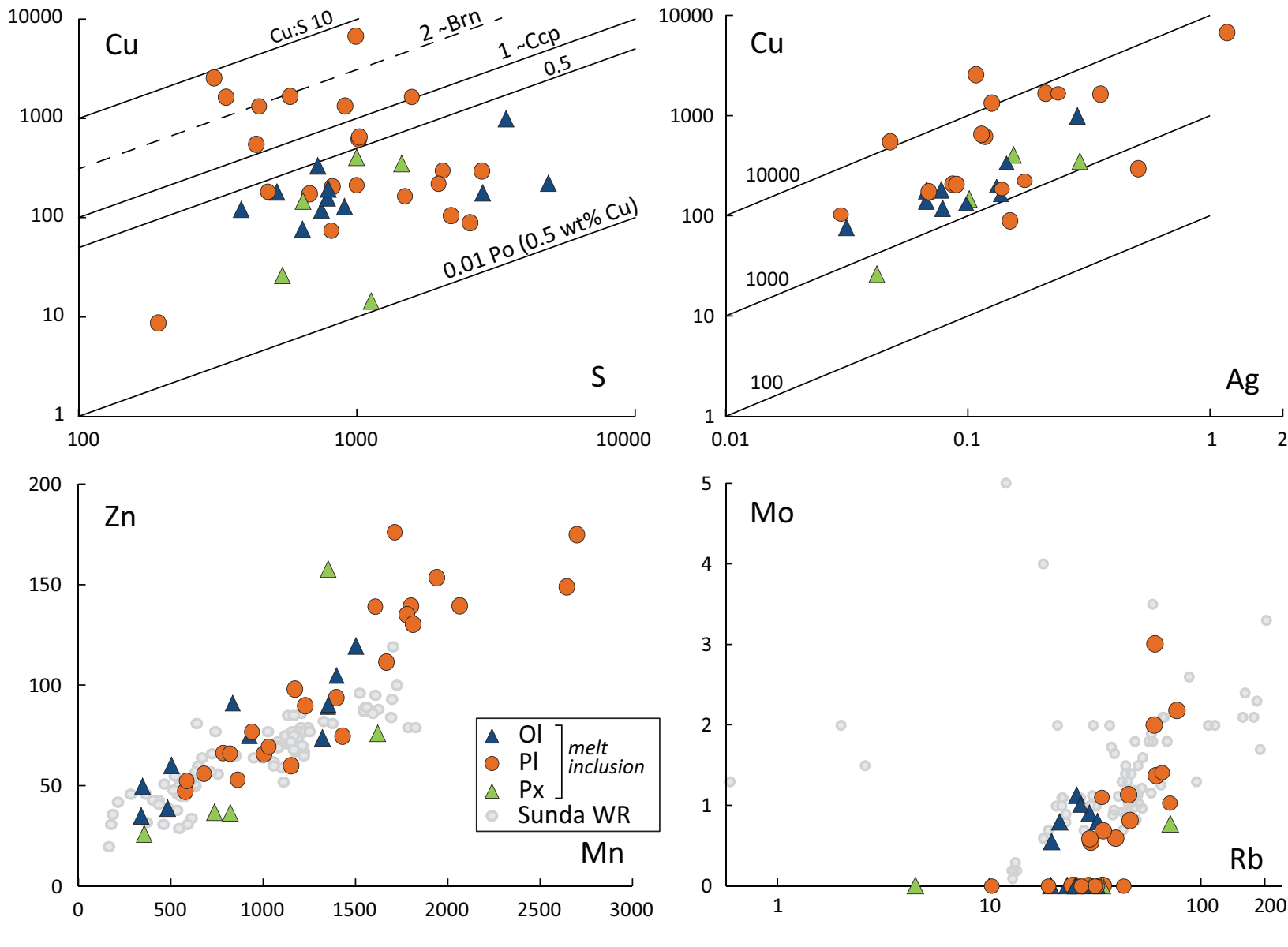

Figure9
Click here to download Figure: Fig9.eps

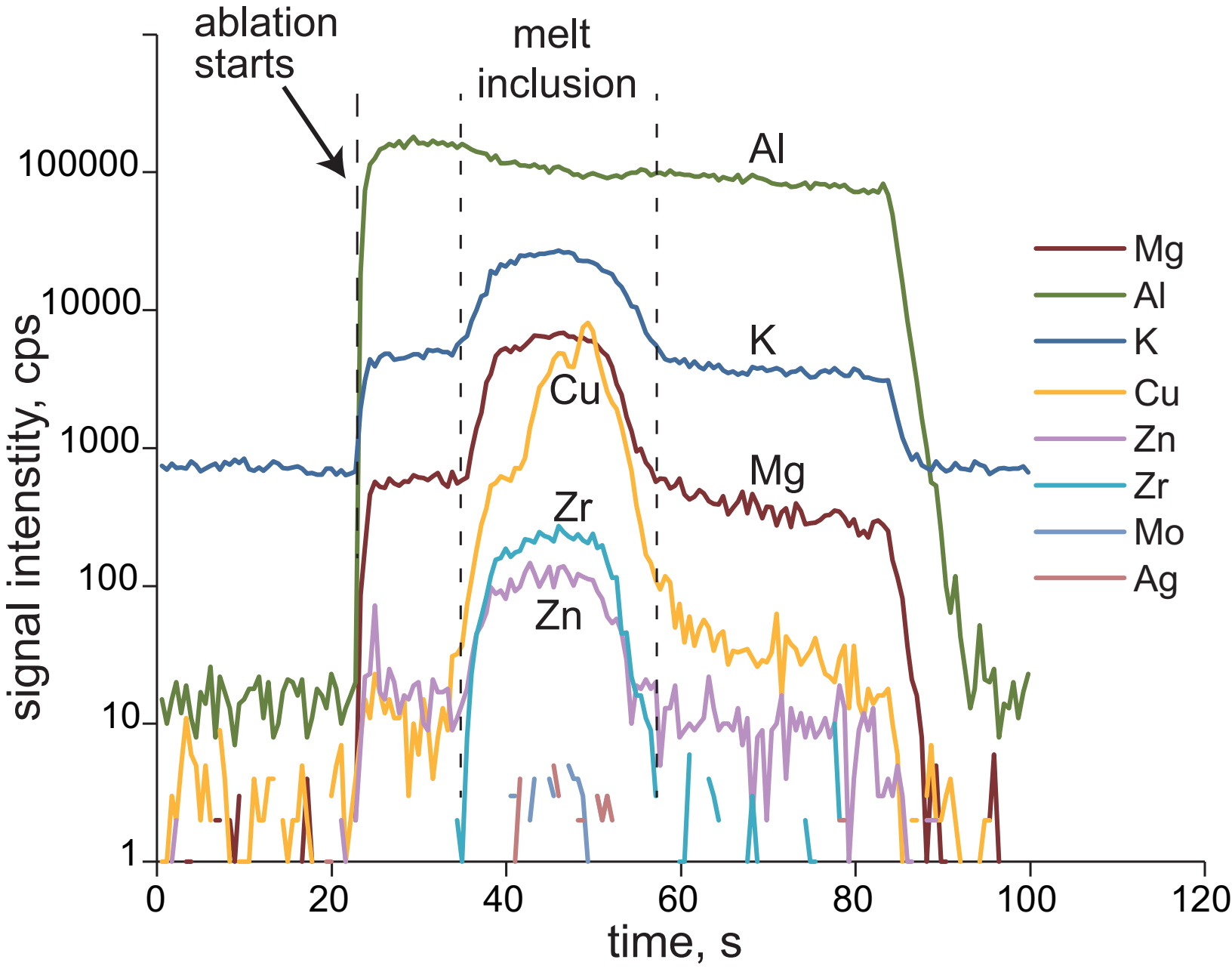

Figure10
Click here to download Figure: Fig10_review.eps

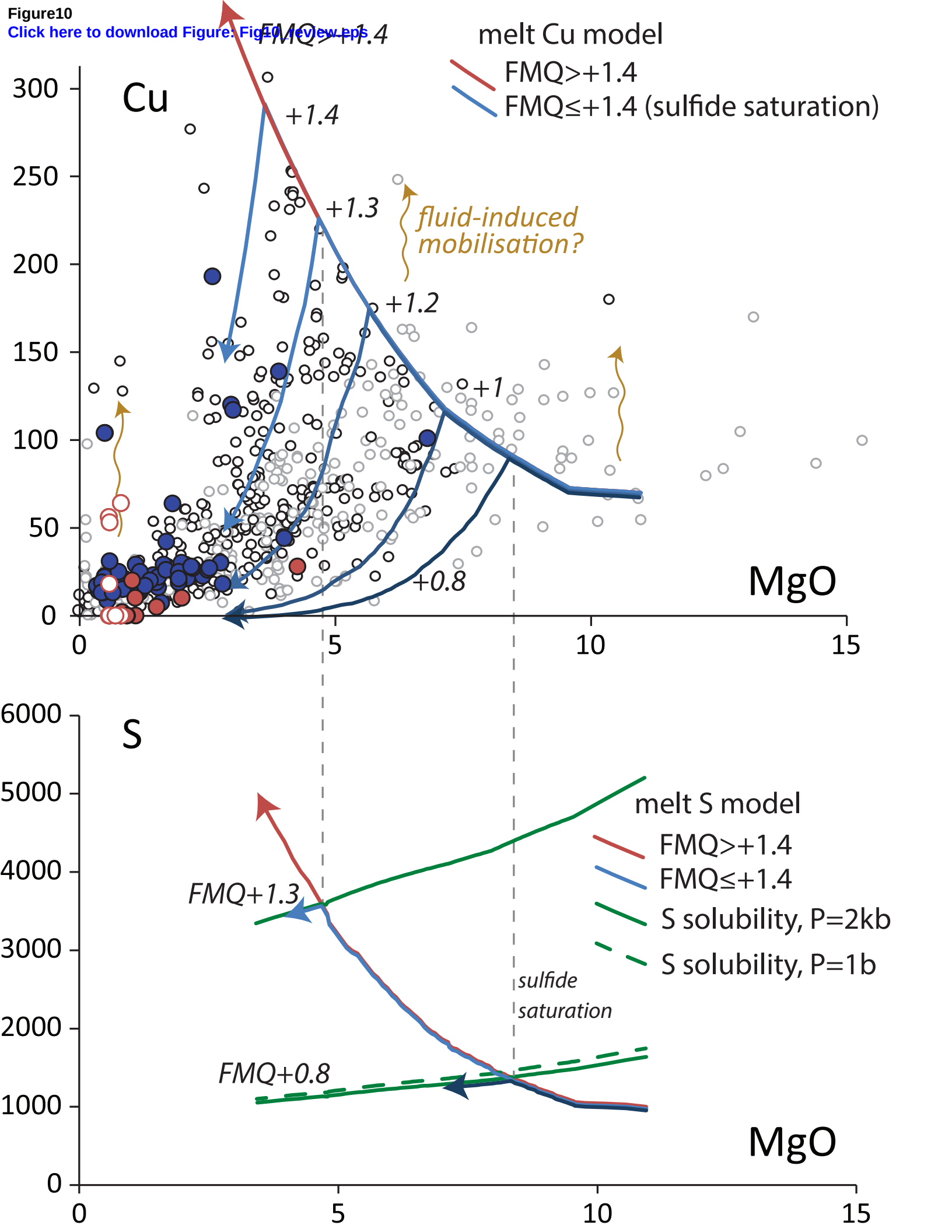

AdditionalFigure1

Click here to download Figure: AddFig1.eps

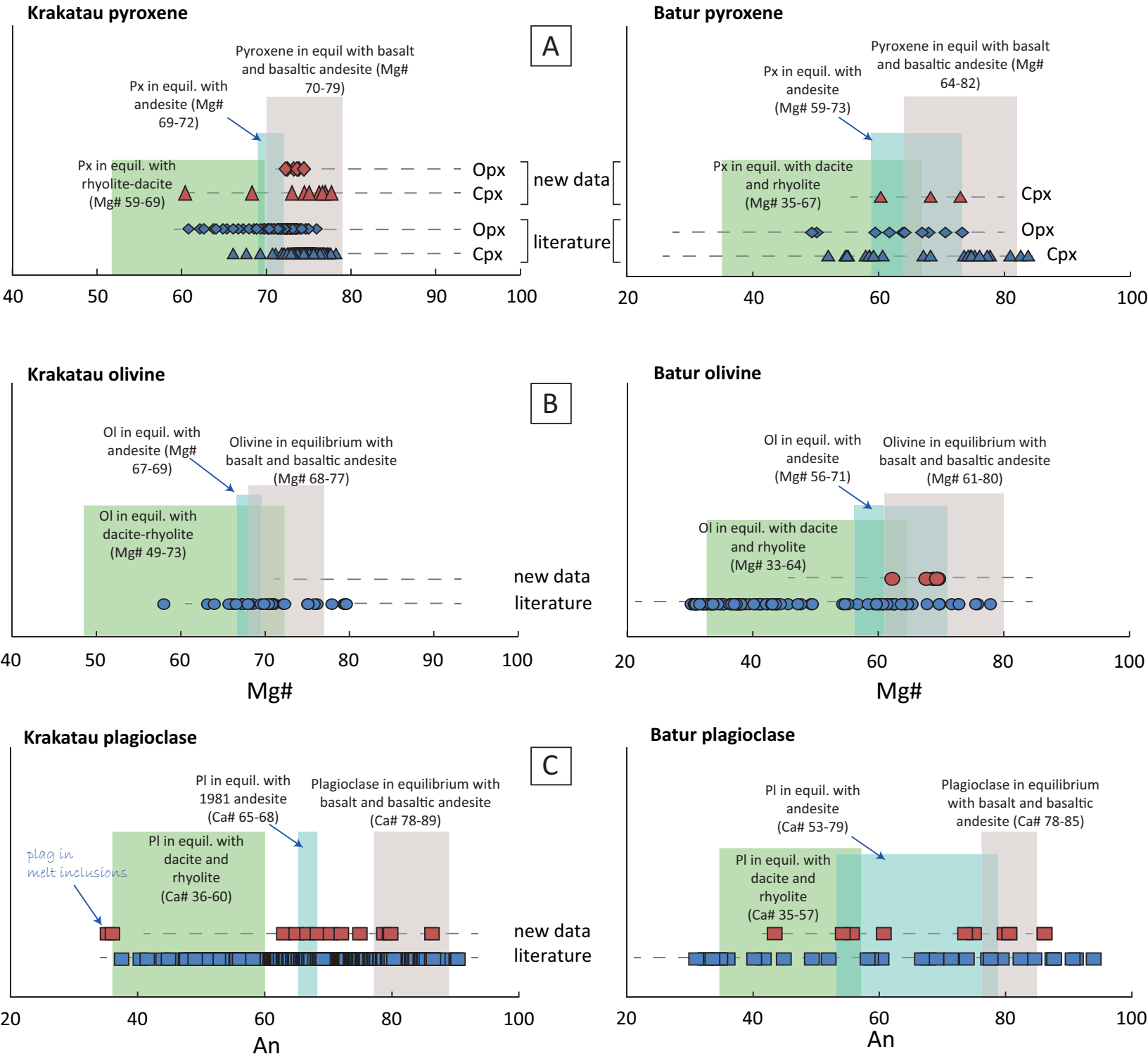

AdditionalFigure2

Click here to download high resolution image

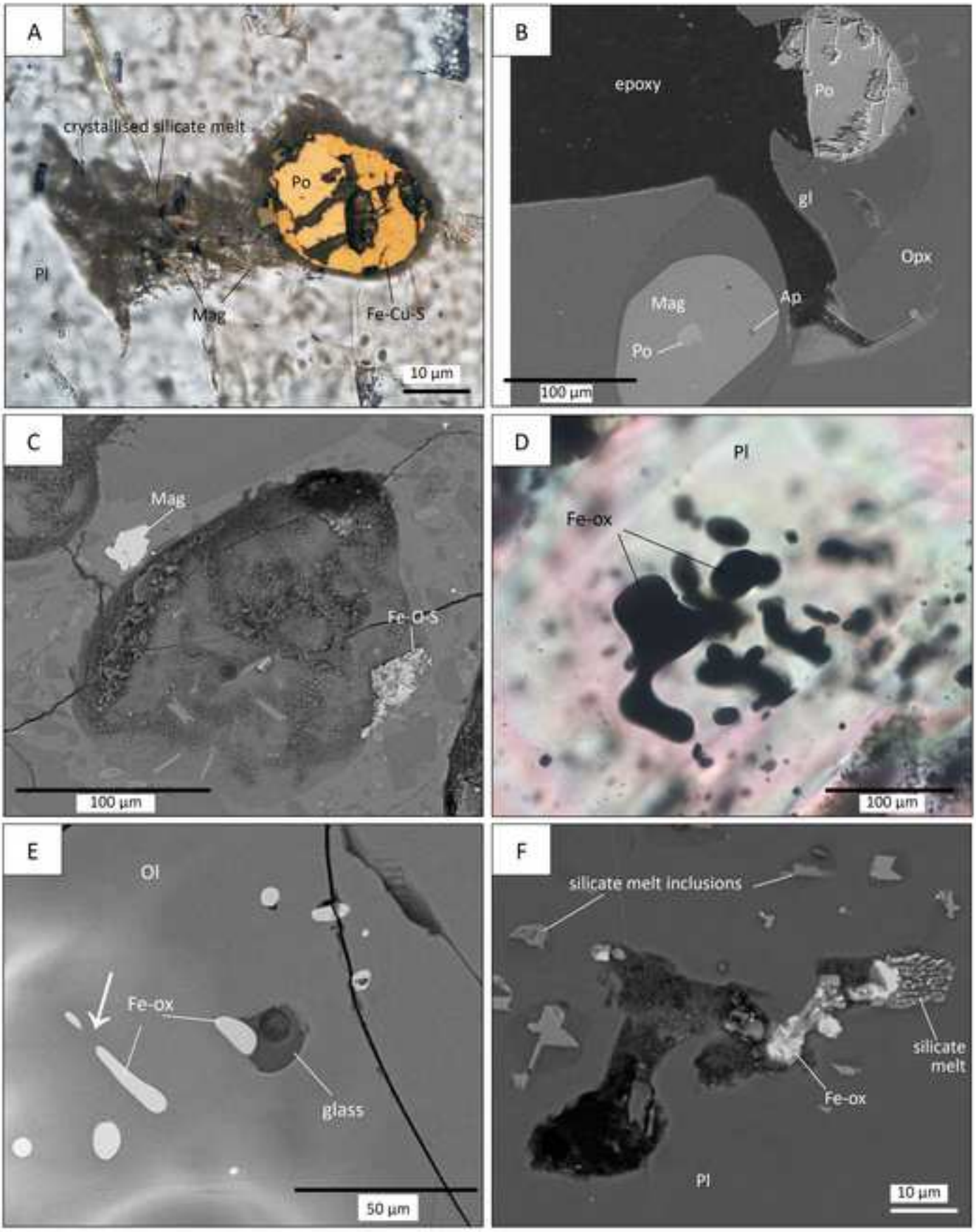

AdditionalFigure3

Click here to download high resolution image